TECHNISCHE UNIVERSITÄT WIEN
Vienna University of Technology

Diplomarbeit

Design and optimisation of a dielectric focusing structure for relativistic electron beams

zur Erlangung des akademischen Grades

Diplom-Ingenieur

im Rahmen des Studiums

Masterstudium Technische Physik

eingereicht von

Jan Anton Hasenbichler, BSc
Matrikelnummer 01229531

ausgeführt am Atominstitut
in Zusammenarbeit mit dem Paul Scherrer Institut in Villigen, Schweiz
unter Anleitung von Dr. Rasmus ISCHEBECK

Betreuung
Betreuer: Privatdoz. Dipl.-Ing. Dr.techn. Michael BENEDIKT

Wien, 27.02.2018

Unterschrift Verfasser

Unterschrift Betreuer

Eidesstattliche Erklärung

Ich erkläre hiermit an Eides Statt, dass ich die vorliegende Arbeit selbständig und ohne Benutzung anderer als der angegebenen Hilfsmittel angefertigt habe. Die aus fremden Quellen direkt oder indirekt übernommenen Gedanken sind als solche kenntlich gemacht.

Die Arbeit wurde bisher in gleicher oder ähnlicher Form keiner anderen Prüfungsbehörde vorgelegt und auch noch nicht veröffentlicht.

Wien, am 27.02.2018

Unterschrift Verfasser

Contents

List of Figures

1 Abstract

Particle accelerators are used in a vast amount of fields in research and industry, everywhere where high energy particles are needed to probe materials, produce radiation for experiments or treatment of patients or simply to test the current understanding of Physics. They typically consist of a huge amount of different components, but most prominently of RF-units to accelerate and dipole and quadrupole magnets to deflect and focus the particles. Though, as conventional particle accelerators, which achieve high energies, are huge and costly to built and operate, a cheap and compact particle accelerator option would be great to revolutionise several fields of research as it would grant access to high energy particles for nearly any laboratory. [3] One idea to solve this problem is the DLA (dielectric laser acceleration). This new type of accelerator design uses the electromagnetic fields of modern lasers in clever combination of dielectric materials to accelerate and focus the particles [4, 5, 6]. This master's thesis focused on optimisation of focusing structures for relativistic electrons in such dielectric laser accelerators within the ACHIP experiment.

As accelerators not only need accelerating structures, but also focusing structures to keep the beam well collimated, the idea of this thesis was to model a laser based focusing structure, do electromagnetic simulations with it and use the discretised electromagnetic fields [7] to simulate the particles propagating through the simulation volume to track their path and deflection. The design of the focusing structure was proposed by Joshua McNeur, a Postoctoral Researcher at the Chair of Laser Physics at the University of Erlangen-Nuremberg who conducted research on a similar design [8]. The construction of the design was done in Autodesk Inventor [9], a computer aided design application for 3D design. The electromagnetic simulations were performed with Lumerical FDTD Solutions [10], a finite difference time domain solver for electromagnetic problems using the Maxwell's equations, because sample files and some experience were already available. The particle tracking code was written from scratch during this thesis in Matlab [11], a numerical computing environment, using a discretised Lorentz force equation and the Boris algorithm for time propagation [7].

The main work of this thesis was about setting up the electromagnetic simulations and the particle tracker for ultra-relativistic electrons, as lower velocities would lead to further difficulties in fabrication, to optimise said focusing structure to figure out the most appropriate design, featuring the highest deflection, the best combined quadrupole like deflection behaviour in both transversal directions as well as not too fragile setup for fabrication. Apart from the computational work, some time was also invested in fabrication possibilities and their limits, possible experiment setups to verify the computational results and theoretical description of the deflection behaviour.

The results of this work include several points. The deflection at highest offsets from the centre increased by up to a factor 60. The so called parallel effect, which shifts the deflection curves independently of the offset depending on the laser phase the particle

enters the structure at was strongly decreased. The behaviour of the structure at two different wavelengths to investigate scaling possibilities of parameters was investigated. Complications when using different refractive indices were described. A mathematical model to figure out the crucial aspects of the electric and magnetic fields was created. Also how deflection in one direction contributes to deflection in the other direction was investigated. Finally first fabrication results and one possible experiment to verify the simulated results were elaborated.

The work has been conducted at the Paul Scherrer Institute, Villigen Switzerland in the Advanced Instrumentation group supervised by Dr. Rasmus ISCHEBECK and Dr. Eugenio Ferrari and lasted from July to end of November 2017.

2 ACHIP experiment

The Accelerator on a Chip International Program (ACHIP) is an international collaboration, funded by the Gordon and Betty Moore Foundation, whose goal is to demonstrate that laser-driven accelerator on a chip can be integrated to fully build an accelerator based on dielectric structures. According to the Accelerator on a Chip International Program at Stanford [5] the collaboration

> includes world-renowned experts in accelerator physics, laser physics, nanophotonics and nanofabrication. The collaboration is led by principal investigators Prof. Robert Byer (Stanford University) and Prof. Peter Hommelhoff (Friedrich Alexander University Erlangen). Three national laboratories – SLAC National Accelerator Laboratory in Menlo Park, California; Deutsches Elektronen-Synchrotron (DESY) in Germany; and Paul Scherrer Institute (PSI) in Switzerland – will contribute expertise and make their facilities available for experiments. In addition to FAU Erlangen, five other universities and one industry partner are involved in the effort: University of California Los Angeles (UCLA), Purdue University, University of Hamburg, the Swiss Federal Institute of Technology in Lausanne (EPFL), Technical University of Darmstadt and Tech-X Corporation.

The idea of laser acceleration was first proposed half a century ago [12] and first demonstrations of acceleration of particles within dielectric nano structures have been achieved as recently as 2013. [13, 14] An example of a possible configuration for a shoebox-sized particle accelerator prototype using dielectric laser accelerators is displayed by ACHIP Stanford [1] in figure 1 and consists of a source, bunchers and first acceleration stages, the additional acceleration stages using the laser driven acceleration and deflectors or undulators as an example application for light generation. With acceleration gradients only limited by the material's damage thresholds exceeding $1GV/m$ this would lead to really compact tabletop accelerators, which could revolutionise research with particle accelerators as it would open access to high energy beams creation even for small laboratories. [3]

Though, as with conventional RF powered accelerators a dielectric laser accelerator does not only consist of acceleration structures. Focusing elements will be needed to keep the electron beam collimated. The idea is to not only use periodic structures for acceleration, but also for focusing as they [15] are capable of providing focusing strengths orders of magnitude higher than for conventional electromagnetic quadrupoles, which would not be appropriate for an accelerator optimised for high current microbunches with significant space charge defocussing. [3]. One of the designs used for focusing are the curved pillars [8], which are the main subject of this thesis.

One of the key points to get an accelerator concept like this to work is precise fabrication and control of the laser's output. Fabrication of such focusing structures is achieved using the vast availability of micro and nano fabrication techniques by the semiconductor

industry [8] or for higher laser damage thresholds dielectrics like fused silica [3]. The typical wavelength used in the ACHIP experiments was chosen as $2\mu m$ [3, 16].

The Paul Scherrer Institute (PSI) will contribute to this by providing the international collaboration access to the high-brightness electron beams in SwissFEL, where it is planned to do a proof-of-principle demonstration of the acceleration of a highly relativistic beam. [16]

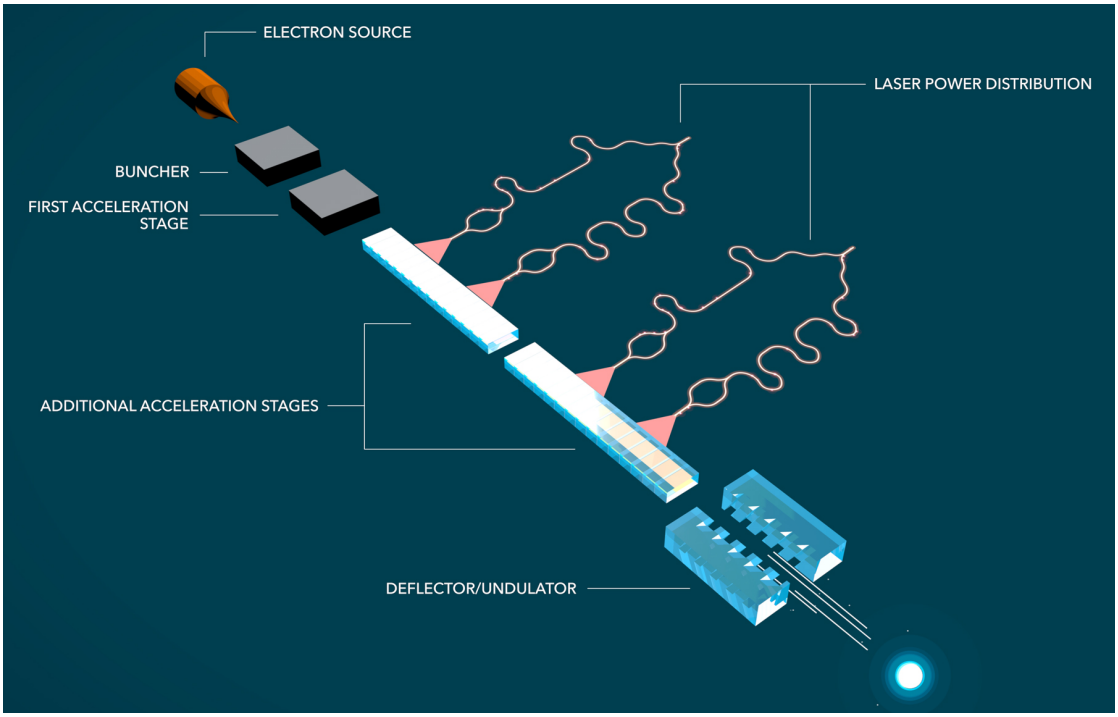

Figure 1: one possible configuration for a shoebox-sized particle accelerator prototype. Image produced by [1]

3 Curved pillar model

The design of the focusing structure used in these simulations was proposed by Joshua McNeur, a Postoctoral Researcher at the Chair of Laser Physics at the University of Erlangen-Nuremberg [17, 18] who conducted research on a similar design [8]. This design consists of three components, the two rows of pillars, the Bragg reflector and a substrate where the pillars and the Bragg reflector are positioned, which in experiments will also be used to mount the structure. A 3D model of the structure is displayed in figure 2.

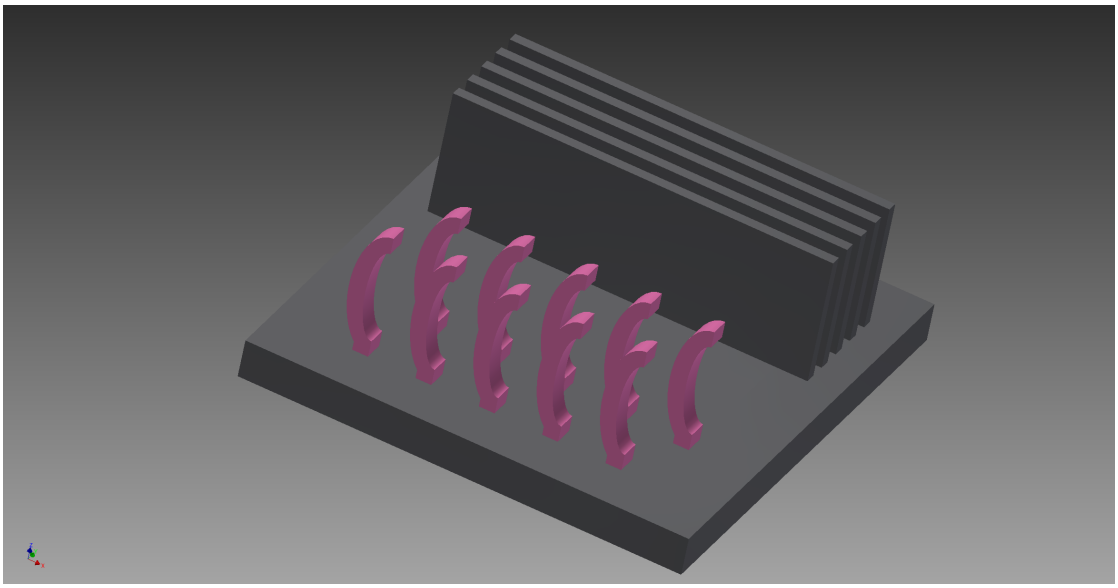

Figure 2: 3D model of the curved pillar model used in the simulations

For later clarity the direction of the coordinate system's axis has to be described. The x-axis is in the direction the particles are propagating. The y-direction is in the direction the laser's light is going. The z-direction is pointed upwards perpendicular to the substrate the pillars and the Bragg reflector are positioned at.

Since the pillars are illuminated by a laser coming from the front side, the Bragg reflector is positioned behind the pillars instead of pumping with the laser from the two sides of the pillars. This suppresses a remaining unwanted transverse component in the electric field between the two pillar's rows. The properties of the Bragg reflector are chosen to fit the incoming laser light to achieve the highest value of reflectivity [19]. Therefore, the Bragg reflector's dimension are only limited by the wavelength and are not part of the optimisation process.

The two rows of pillars are characterised by a large number of parameters to be optimised. The structure's parameters are the width of the pillars, the gap between the two rows of pillars, the shift between the front row and back row of pillars (which can

be seen in figure 3) and the height of the pillars which is measured from the substrate up to the highest point of the pillars. The initial value for the pillar shift is half of the wavelength as the distance between two pillars in the same row is one wavelength. This shift is referred to as a shift of 0 nm in this thesis and the result plots. There are two parameters left, which are defined by the way the pillars are constructed. The pillars consist of two ellipses. One is the outer and therefore bigger ellipse, whose semi major axis is bound by the height of the pillars and its semi minor axis is bound by half of the wavelength. The only two parameters to be optimised are the sizes of the semi major and semi minor axis of the inner ellipse. The position of the inner ellipse compared to the outer ellipse could be optimised too, but this would add asymmetry in z-direction, which is to be avoided. In this case the difference between the semi major and minor axis of the outer ellipse compared to the axes of the inner ellipse was chosen as two parameters. The difference between the two semi major axes is called *curvature a*. Using the same naming convention the difference between the two semi minor axes is called *curvature b*. A display on how the ellipses are changed by the two parameters each on their own or both symmetrically at the same time can be seen in figure 4 - 6.

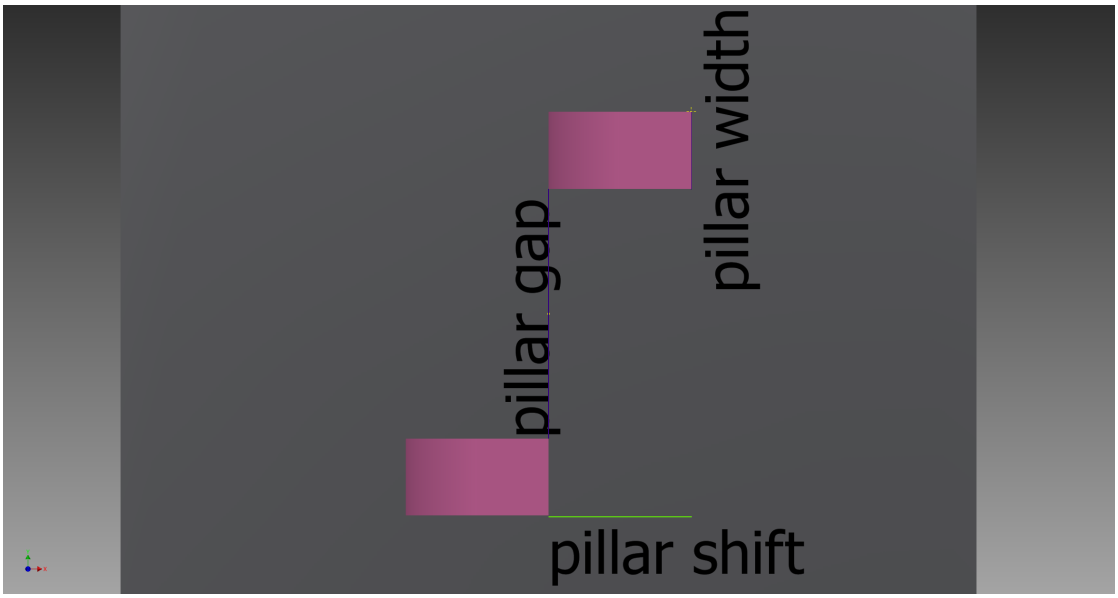

Figure 3: Parameter description top view of the curved pillars

All the parameters described were tested and optimised during this thesis.

3.1 Pillar head for improved symmetry

Since the results showed some asymmetries, as described in section 7 and most prominently seen in figure 24, the effect of the pillar's leg was tested. The results showed, that removing the leg removes these asymmetries. Since the leg is needed for stability, a head was added on top of the pillars with the same dimensions as the leg as seen in figure **??**.

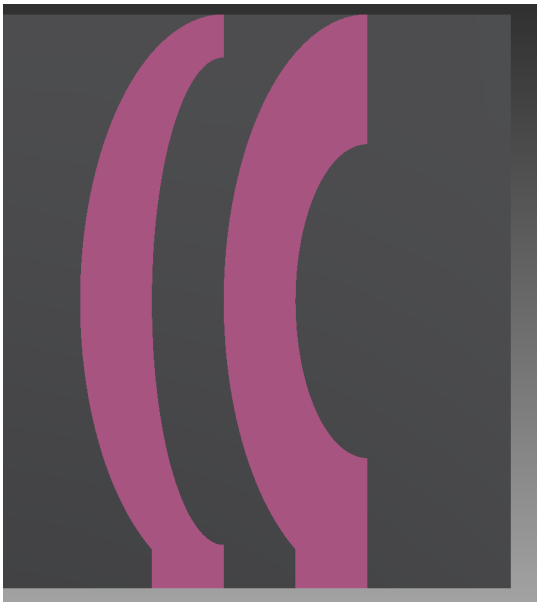

Figure 4: Displaying the difference the curvature a parameter has on the structure

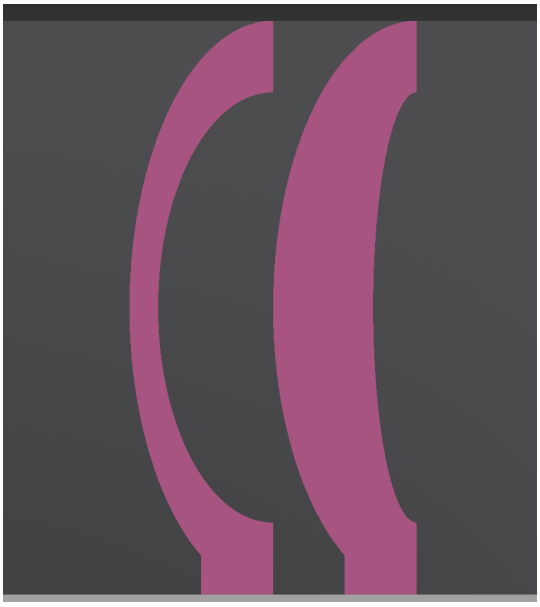

Figure 5: Displaying the difference the curvature b parameter has on the structure

Figure 6: Displaying the difference a symmetric change of parameters has on the structure

Figure 7: Pillar head for improved symmetry

This head had the same effects as removing the leg and therefore the asymmetries were solved also increasing the stability of the pillars. The head was used in 3.3 μm pillar

shift test in section 7.7 and in all 2 μm tests except the pillar width and the pillar gap test as these were done before the effect of the pillar head was found.

3.2 Different possible curved pillar models

The curved pillar model optimised in this thesis is just one possible proposal for a focusing structure. Some thoughts were put into three further models. Two of these models are variations of the optimised model and one is an idea taken from a paper by Kent Wootton [2] and tweaked to fit the simulation setup.

The first variation of the optimised model is the full curved pillar model as seen in figure 8. In this model the front pillars perfectly align with the back pillars. From the laser's point of view there is no free space between the laser and the Bragg reflector. This model has less tweakable parameters as the pillars are constructed using two equal ellipses. Therefore, apart from the standard parameters height, width and pillar gap the only tweakable curvature parameter would be the semi minor axis of the two ellipses. In the initial design the shift between the front and the back row of pillars was half of the wavelength. Without simulations it is not clear if shifting this design would make a change in the deflection results as from the laser's point of view there is no free space between the laser and the Bragg reflector.

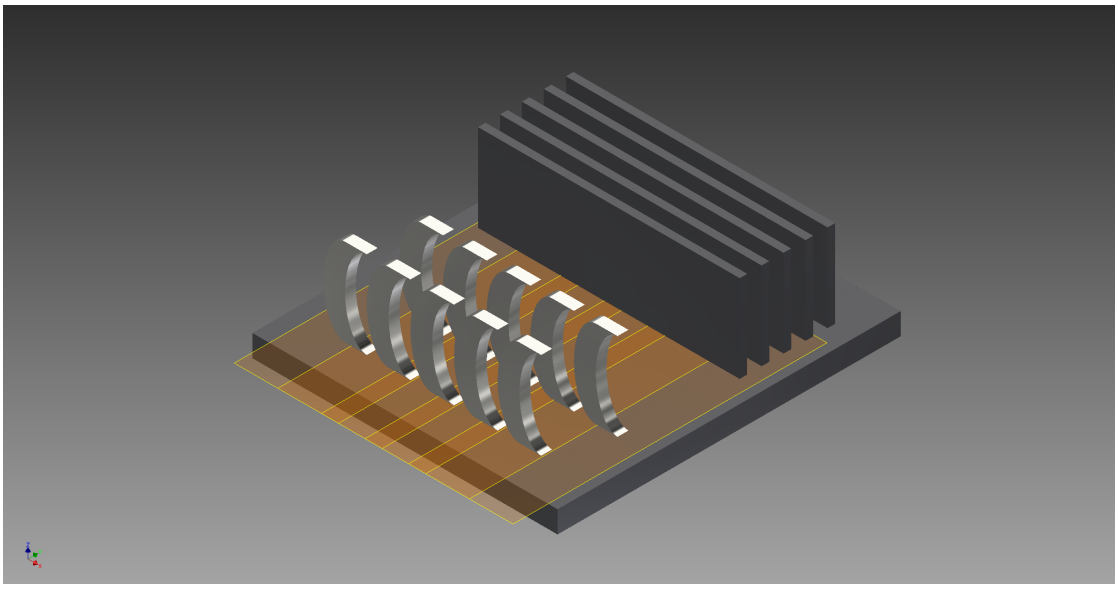

Figure 8: 3D model of the full curved pillar model

The second variation of the optimised model is the inward curved pillar model as seen in figure 9. In this model the front pillars perfectly align with the back pillars as with the full curved pillar model. Again, from the laser's point of view there is no free space between the laser and the Bragg reflector. Except for the shift, which might also not

change the deflection results, the tweakable parameters are the same as in the optimised model as the pillars are constructed using two ellipses.

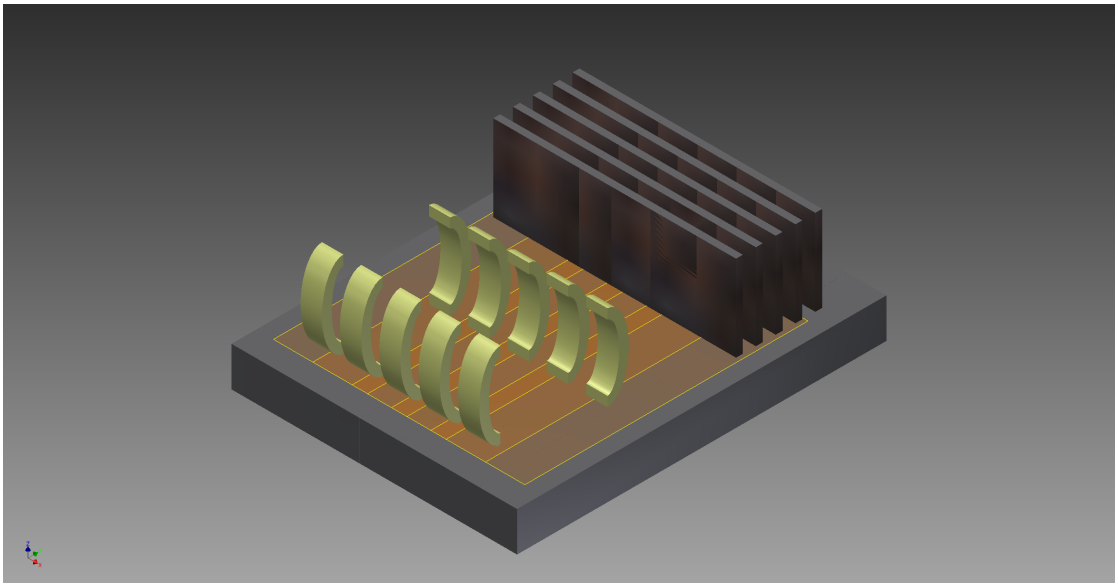

Figure 9: 3D model of the inward curved pillar model

A third possibility, not explored in this thesis, is the checkerboard-like design [2] as seen in figure 10.

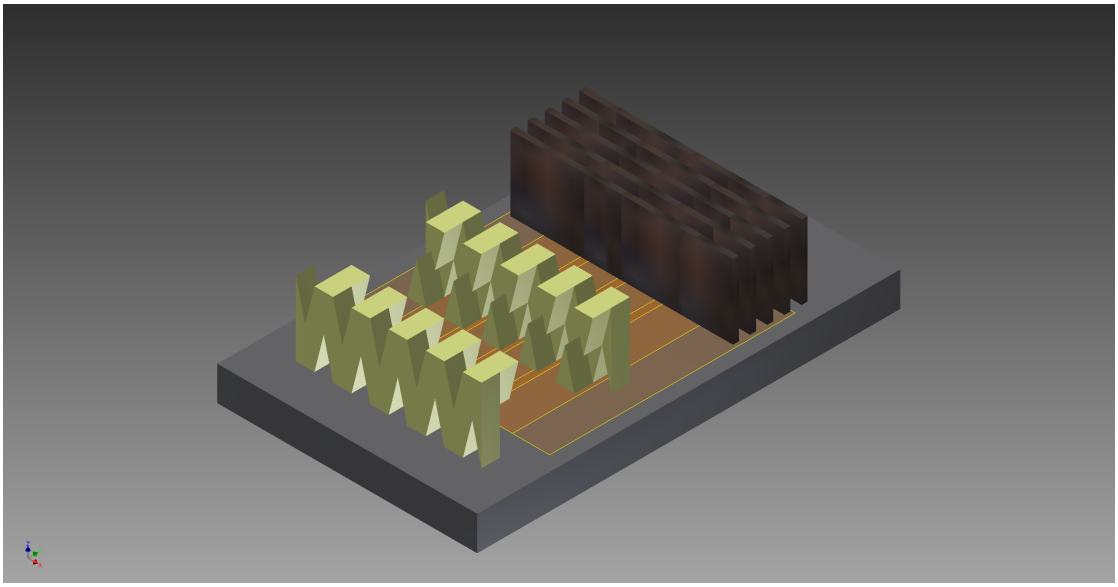

Figure 10: 3D model of the checkerboard structure [2]

4 Autodesk Inventor

All the design and construction of the different models and especially the optimised model was done in Autodesk Inventor [9]. Inventor was mainly used because it is the standard construction tool at Paul Scherrer institute and therefore questions could easily be solved onsite. The only requirement is, that the program is able to export the construction into an STL file type, which tesselates the 2D outer surface of the structure using triangles [20]. The STL file type is needed to import the model into Lumerical as seen in section 5.

The curved pillar model consists of three parts in Inventor. These parts are the Bragg reflector, the front pillar and the back pillar. For 3D printing or fabrication there is also a fourth part, the substrate, but for simulation purposes this was not included into the STL files. To optimise the simulation speed only one period containing one front pillar, one back pillar and a small part of the Bragg reflector was constructed. This unit cell was exported into an STL file for simulation purposes as periodic boundary conditions were used. For 3D printing or fabrication purposes this unit cell was multiplied to receive the desired amount of pillars.

As the perfect position of the Bragg reflector was not known in the early beginning of this work and changing the position of the reflector in Inventor, exporting it into an STL file, importing it into Lumerical and redoing the electromagnetic simulations to find out, if the new positioning is correct, takes far more time than to set up a Bragg reflector in Lumerical and changing the parameters there, also the Bragg reflector typically was not included into the STL files. For further tests or constitutive projects this could easily be done as the perfect position of the Bragg reflector did not change anymore.

5 Lumerical

Lumerical is a finite difference time domain solver for electromagnetic problems using the Maxwell's equations [10]. As seen in figure 11 the workspace consists of four windows. Three of these windows show two dimensional projections of the model and the fourth shows a three dimensional model. A full construction of the desired model can be created using Lumerical's tools, though in this case only the Bragg reflector was built within Lumerical since the curved pillars were imported via an STL file from Autodesk Inventor.

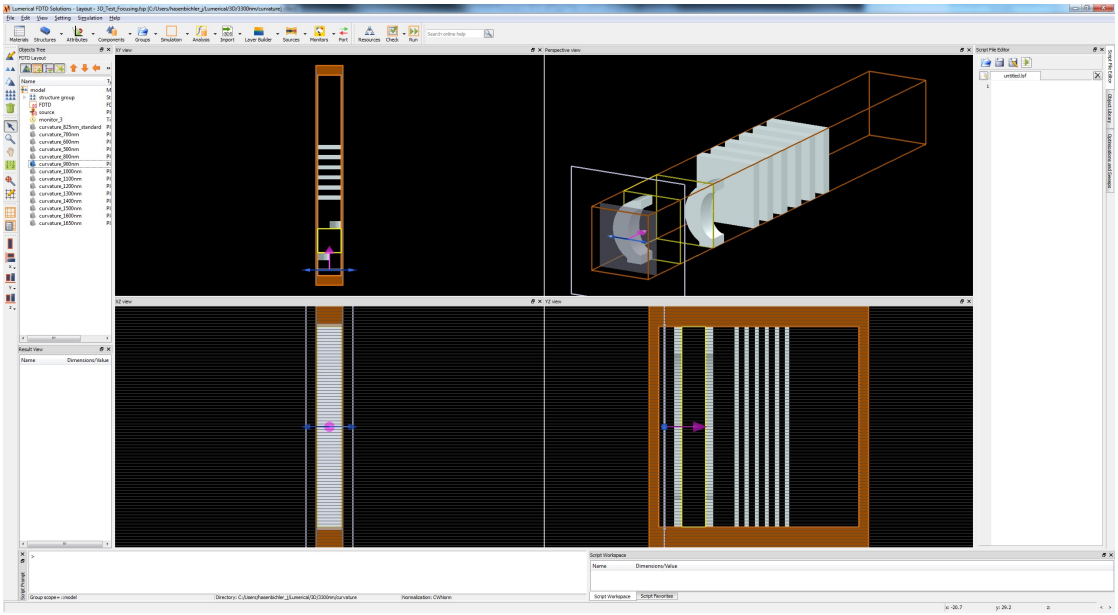

Figure 11: overview of Lumerical's workspace

The typical setup consists of the curved pillars, the Bragg reflector, a laser source, the FDTD simulation volume and a monitor to record the data.

The FDTD simulation volume defines parameters like its geometry, the background refractive index, the simulation time, simulation temperature, mesh settings and boundary conditions. For all simulations these parameters were a background refractive index of $n = 1$, a simulation time of $t = 3000\,\mathrm{fs}$, a simulation temperature of $T = 300\,\mathrm{K}$, a mesh size of 14 points per wavelength, periodic boundary conditions in x-direction and perfectly matched layers in y and z-direction.

The source options defines properties like source shape, amplitude, injection axis, polarisation angle, geometry, wavelength and pulse options. For all simulations these parameters were a plane wave with an amplitude of one, injected in y-axis with a polarisation angle of 90°. This means that before the laser hits the pillars it's polarised in a way, that the electric field in x-direction and magnetic field in z-direction are non zero. The laser is positioned before the front pillar with a wavelength of either $\lambda = 2\,\mu\mathrm{m}$ or $\lambda = 3.3\,\mu\mathrm{m}$

and a pulse length of 30 000 fs with a maximum at 2980 fs. This pulse length and maximum position was chosen to have a well irradiated simulation volume and a constant laser source by the time the monitor starts recording the data.

The monitor defines parameters like the start and stop time of the recording, the geometry, which components of the fields are recorded and using a sample rate per cycle together with the mesh size and a stability factor in the FDTD simulation setup to calculate the number of snapshots during the start and stop time. The geometry was placed between the two pillars with an y-dimension of the pillar gap, the x-dimension of one wavelength and the z-dimension of the height. The start and stop time was set to record for three full periods and therefore between 2970 fs and 2990 fs for a wavelength of 2 μm and between 2960 fs and 2993 fs for a wavelength of 3.3 μm. All components of the electric and magnetic field were recorded and the sampling per cycle was tweaked together with the stability factor to get 14 points per wavelength and therefore 43 points for the whole recording time.

After the electromagnetic simulations are completed and recorded with the monitor, results can be exported using the command *matlabsave*.

5.1 Mesh size determination

The size of the mesh grid defines the accuracy of the simulation since more points per wavelength mean more continuous solving of the equations. To determine how many points per wavelength are needed to achieve less than a desired amount of numerical error a small test was created. The test consisted of a trapezoidal rule algorithm [21] calculating the area under a sine wave. A sine wave was chosen because the changes in the electric and magnetic field are described by a sine and cosine wave. This discretised area is then compared to the analytical area under a sine wave and a relative error is calculated. The relative error has been chosen to be 1%. As seen in figure 12 this is achieved by using 14 points per wavelength. Although lumerical uses far more sophisticated algorithms to solve the electromagnetic problem, which might hit the one percent hurdle with less points per wavelength as their error is of a higher order than the trapezoidal rule's order of one, this small test gave some good insight, that even in worst case scenarios the numerical error should not be higher than one percent. Therefore, for all the simulations time wise an amount of 14 points per wavelength was chosen. Spatially the refractive index has to be considered in this as well. Since the wavelength is smaller within the material, the amount of points per wavelength has to be multiplied by the refractive index to have the same accuracy also within the material. Therefore, the full simulation volume was simulated with about 20 points per wavelength to account for the material's refractive index.

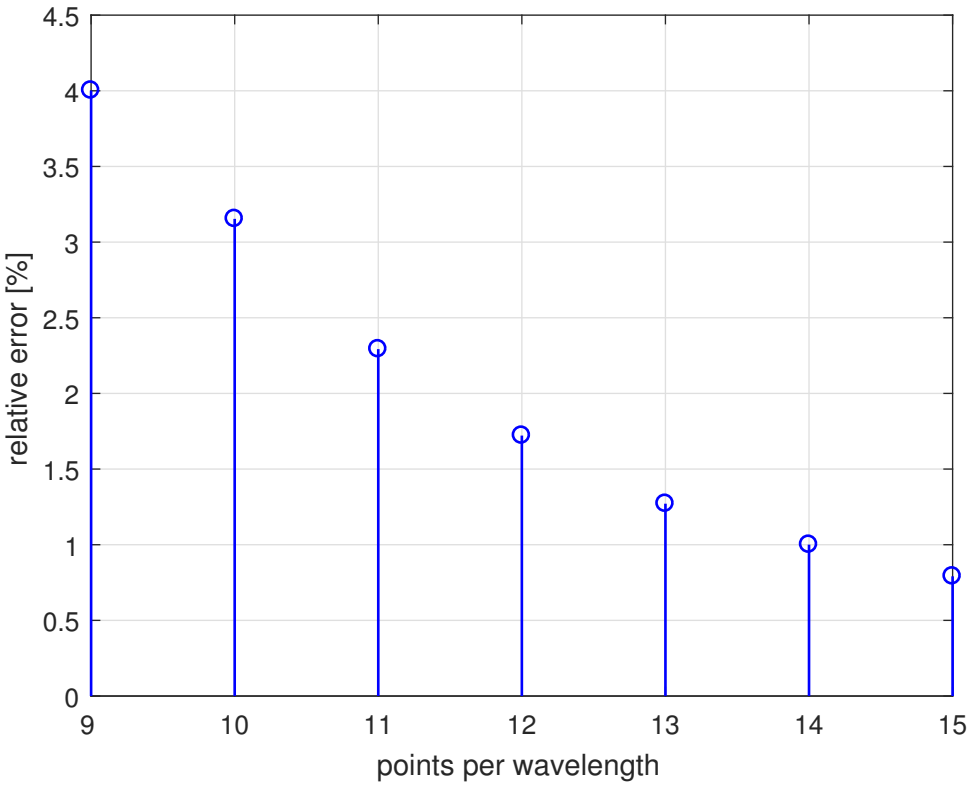

Figure 12: relative error of Trapezoidal rule discretising one period of a sine wave

5.2 Bragg reflector dimensions and positioning

The important property of the material to define the dimensions of the Bragg reflector is its refractive index. As fused silica or glass was used as material, the refractive index was $n = 1.438$ for the $\lambda = 2\,\mu$m simulations and $n = 1.411$ for the $\lambda = 3.3\,\mu$m simulations using an interpolation of the values found in the Handbook of Optical Constants of Solids [22].
The Bragg reflector [19] is composed of two alternating materials with different thicknesses of

$$d = \frac{\lambda}{4n}. \tag{1}$$

One material was fused silica and the other was vacuum, the gap between two walls of fused silica was a quarter of the wavelength corresponding to $d_2 = 500\,$nm for the $\lambda = 2\,\mu$m simulations and $d_2 = 825\,$nm for the $\lambda = 3.3\,\mu$m simulations. The fused silica walls therefore were further decreased by their refractive index corresponding to $d_1 = 347.7\,$nm for the $\lambda = 2\,\mu$m simulations and $d_1 = 584.7\,$nm for the $\lambda = 3.3\,\mu$m simulations. As such accuracies in fabrication presently can not be achieved, $d_1 = 348\,$nm for

the $\lambda = 2\,\mu$m simulations and $d_1 = 585\,$nm for the $\lambda = 3.3\,\mu$m simulations were chosen in Lumerical's setup.

The positioning of the Bragg reflector was done plotting the $z = 0$ slice of the magnetic field in z-direction at the time point, where the peak to peak field strength in the data acquisition volume inbetween the pillars was strongest. As seen in figure 13, where the range in colour is close around zero field strength, the minimum oscillates in y-direction slightly above and below the $2\,\mu$m point as the x position increases. Though, the average is exactly at $2\,\mu$m. The magnetic field in z-direction was arbitrarily chosen to align the Bragg reflector. The same can also be done plotting a range in colour close to the maximum for the electric field in x-direction as seen in figure 14. The other two directions of the two fields might be used as well, but since the laser is polarised in x-direction for the electric field and in z-direction for the magnetic field, these directions are preferred.

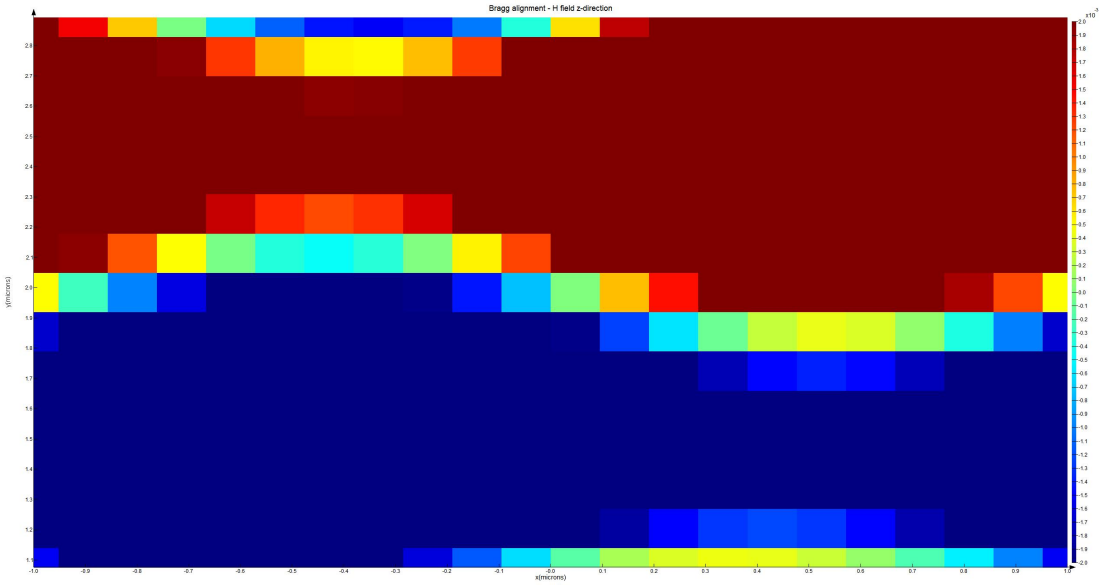

Figure 13: magnetic field strength in z-direction showing perfect alignment of the Bragg reflector

5.3 Perfectly Matched Layers

Perfectly matched layers are artificial layers introduced in Lumerial's simulations to absorb every incoming wave by simulating a wave propagating into unbounded regions. This is needed to achieve a simulation without any reflections [23]. In this model perfectly matched layers are used at the upper and lower end of the model in y and z-direction to mimic the laser beam outflowing and disappearing. Though, while the perfectly matched layers in y-direction were positioned close before the incoming laser and some

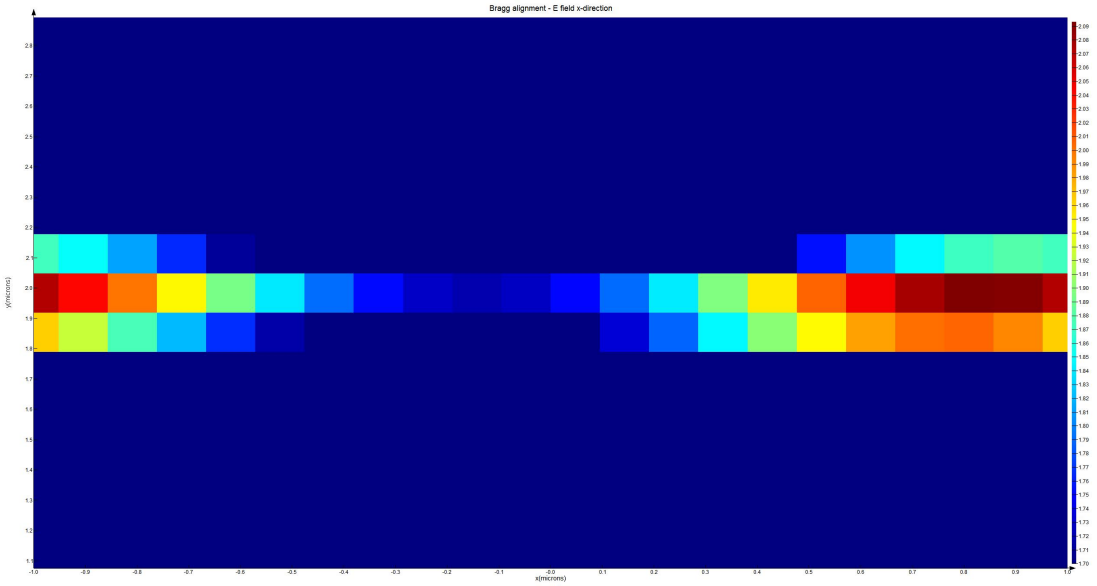

Figure 14: electric field strength in x-direction showing perfect alignment of the Bragg reflector

micrometers behind the Bragg reflector, in z-direction still some reflections were visible in the simulation volume. To prevent this, the simulation volume in z-direction was symmetrically extended fifteen fold to get rid of all the remaining reflections. For further simulations also including the substrate it might be advisable to add the perfectly matched layers below a small amount of substrate to reduce simulation time as the perfectly matched layers have the same properties as the adjacent material.

6 Particle tracking code

The particle tracking code was written in MATLAB [11] and uses the discretised electromagnetic field data from Lumerical to track a particle's path while propagating through the pillars. Solving the equations of motion is done by discretising the Lorentz force equation and time integrating using the Boris algorithm [7]. After the particles have passed the last pillar, their angle compared to their initial angle is calculated. Since all deflection tests were done with an incident angle of 0° the deflection angle was compared to the path the particle would propagate without the laser turned on. The deflection angles are recorded and plotted as a function to the particles injection position.

6.1 data structure and interpolation

Lumerical's exported MAT file consists of a structure that includes electromagnetic field data and data grid points for spatial and time dimensions. The data is in the shape of a three dimensional matrix. The amount of slices is equal to the amount of time wise mesh points. Since three periods were sampled this typically amounted to 43 slices. The amount of columns is equal to the amount of field directions recorded. In all cases all three field directions were recorded, so there are three columns in the data. The amount of rows is equal to the multiplication of the amount of mesh points in x, y and z-direction. Therefore, the rows have to be reshaped to access them like a matrix.

Since the data is discretised and is only available at specific data grid points, but the particles will spatially also hit positions between two data grid points, spatial interpolation is needed. This is done by linear interpolating the field between the two data points. If times steps smaller than the time wise data grid is used, also time wise interpolation is needed. The procedure is the same as in the spatial case. Overall the field felt by the particle on its path through the pillars is a linear interpolation of the adjacent spatial data grid points and the time wise data grid points.

6.2 Lorentz force discretisation and Boris integration

To describe the interaction of the fields with the particles the Lorentz force has to be discretised and an appropriate time integration has to be chosen to advance in time. In this thesis the Boris method or Boris rotation was used [7].

The relativistic Lorentz force, as the simulations are done for ultra-relativistic electrons with $0.9999c$ is described by

$$\vec{F} = \frac{d}{dt}\left(\gamma m \vec{v}\right) = q\left(\vec{E} + \vec{v} \times \vec{B}\right) \qquad with \qquad \gamma = \frac{1}{\sqrt{1 - \frac{v^2}{c^2}}} \tag{2}$$

where F is the force, γ is the Lorentz factor, m is the electron's mass, v is its velocity, q is its electric charge, E is the electric field and B is the magnetic field. Discretising the differential time step makes it necessary to average the velocity over two time steps.

With the definition of $u = \gamma v$ the equation in its discretised form (n being the integration step and Δt being the time step) is

$$\frac{u^{n+\frac{1}{2}} - u^{n-\frac{1}{2}}}{\Delta t} = \frac{q}{m}\left(E^n + \frac{u^{n+\frac{1}{2}} + u^{n-\frac{1}{2}}}{2\gamma^n} \times B^n\right). \tag{3}$$

Note that in reference [7] the magnetic part of the equation is divided by the speed of light c. This is due to the fact, that a different unit system is used. Since the electric and magnetic fields are simulated in SI-units [24], the SI form of the Lorentz equation is used. To separate the electric and magnetic forces completely [25] the velocities are substituted by

$$\begin{aligned} u^{n+\frac{1}{2}} &= u^- - \frac{qE^n\Delta t}{2m} \\ u^{n-\frac{1}{2}} &= u^+ + \frac{qE^n\Delta t}{2m} \end{aligned} \tag{4}$$

which results in a Lorentz force equation without the electric field

$$\frac{u^+ - u^-}{\Delta t} = \frac{q}{2\gamma^n m}\left(u^+ - u^-\right) \times B^n. \tag{5}$$

The B field rotation can be done using two

$$\begin{aligned} u^{'} &= u^- + u^- \times t \\ u^+ &= u^- + u^{'} \times s \end{aligned} \tag{6}$$

with $t = \frac{qB\Delta t}{2\gamma m}$ and $s = \frac{2t}{1+t^2}$. A geometric description of this rotation can be seen in reference [7] on pages 60 to 62. To advance in position the time has to be integrated according to

$$x^{n+1} = x^n + v^{n+\frac{1}{2}}\Delta t = x^n + \frac{u^{n+\frac{1}{2}}\Delta t}{\gamma^{n+\frac{1}{2}}} \qquad with \qquad \left(\gamma^{n+\frac{1}{2}}\right)^2 = 1 + \left(\frac{u^{n+\frac{1}{2}}}{c}\right)^2. \tag{7}$$

A pseudocode of the whole algorithm can be seen at algorithm 1. It has to be noted, that the first part of the the pseudocode is to make use of the periodic boundary conditions of the simulations. Since the electromagnetic simulations only account for one pair of pillars, if the particle reaches the end of the first pair, the field data from the beginning of the first pair is used for further tracking. This is therefore similar to the behaviour of when the time step exceeds one period.

6.3 offset test setup and perfect phase definition

Since the idea is to get focusing effects with this structure, a test to track the focusing abilities had to be created. This was done by defining a path, where a particle, if it is

Algorithm 1 pseudocode of the particle tracking algorithm

```
1: procedure particleTracking
2: loop:
3:     if position y or z > ymax or zmax then return end of tracking
4:     if particle position outside x boundary then
5:         totalx = totalx + x
6:         x = x − xmax
7:         if total path in x > amount of pillars * xmax then return end of tracking
8:     interpolate E and B field
9:     calculate u^−
10:    calculate γ^−
11:    calculate t and s
12:    calculate u' and u^+
13:    calculate u^{n+1/2}
14:    calculate γ^{n+1/2}
15:    calculate x^{n+1/2}
16:    goto loop.
17:    α_y = arctan v_y/v_x
18:    α_z = arctan v_z/v_x
```

following this path, is not deflected at all. Since the coordinate system center in Lumerical has been chosen to have this path at both the centre in y and in z-direction meaning symmetrically between the two rows of pillars and at half height of the pillars, this point was called the centre point. If the particle is inserted at the centre point its deflection should be minimal or ideally even zero. To test how the field acts on the particle, if the particle is off centre, the offset test was created. It consists of tracking the deflection angle in y-direction and in z-direction for different amounts of offsets from the centre. The typical setup is, that for a y deflection test, the z-position is kept at the centre and the y-position is changed and vice versa if a z deflection test is done. The typical offset values are $-0.625\,\mu$m to $0.625\,\mu$m in y-direction and $-1.25\,\mu$m to $1.25\,\mu$m in z-direction as in the initial design the height was twice as big as the pillar gap. Though, in some later tests especially with $2\,\mu$m wavelength the maximum offset was decreased as the particles were two close to the pillars. Some small variations of this test were done throughout this thesis and will be described in the following. Though, the initial concept of tracking the deflection angle at different offsets stayed the same.

Important for the offset test is obtaining the perfect phase. The perfect phase in this thesis is defined differently for tests in y-direction than it is for tests in z-direction. In z-direction the perfect phase is defined as the phase, where the deflection is the highest. Since the deflection curve is not perfectly linear the perfect phase point for smaller offsets might be different than for greater offsets. This was the case in the $2\,\mu$m tests with smaller pillar gaps when the maximum offset was decreased and the perfect phases had

to be re-obtained. Though, to have a fixed definition the perfect phase is defined as the phase where the deflection for the greatest positive and negative offsets is the highest. In y-direction, instead, the perfect phase is defined as the phase, where zero offset produces zero deflection. This difference in definition is caused by the so called *parallel effect* and will be further described in section 7, 8 and 10.

Also it has to be noted, that for each direction there are two phase points which could be considered perfect. One phase point is, where the deflection curve shows focusing and one where the curve shows defocusing behaviour. These two phase points are typically half a period shifted, but especially in the y-direction this is not always the case. Also, if the pillars produce a quadrupole like deflection the focusing phase point in z-direction should align with the defocusing phase point in y-direction and vice versa effectively only generating two perfect phase points instead of four.

6.4 incident field strength test

Since Lumerical typically does all its electromagnetic simulations with an amplitude of 1, the actual amplitude was added in the particle tracking code by multiplying the field data by the desired strength. In the simplified model used in this thesis, where non linear effects are neglected, the field amplitude of the electric and magnetic field is a multiplication factor in the Lorentz equations. Therefore it does only change the magnitude of the solutions of Maxwell's equations, if a different starting amplitude of the plain wave is chosen. Though, the amplitude of the fields is important for the particle tracking, as a higher amplitude acts as a stronger force on the particle. A reasonable field strength for the laser in possible experiments is $1\,\mathrm{GV/m}$. [8] The deflection of the particles is supposed to scale with the amplitude of the electric and magnetic field or quadratic in power as $|S| = \epsilon_0 c^2 |E| \cdot |H|$. [26] Hence, the deflection behaviour should scale by the same factor as the amplitudes.

Therefore, a test on the reliability of the code was the incident field strength test by looking at the deflection angle for different offsets at different field strengths. The tested incident strengths varied between $0.1\,\mathrm{GV/m}$ and $10\,\mathrm{GV/m}$. The results are displayed in figure 15 and 16 and show a clear expected linearity at all tested offsets. This proved, that nothing was conceptionally wrong with the particle tracking code.

All further tests and simulations were conducted using a field strength of $1\,\mathrm{GV/m}$, but future these results are still valid, if in future experiments lasers with higher field strength are used, as the deflection results in our approximation will scale linearly with the field strength.

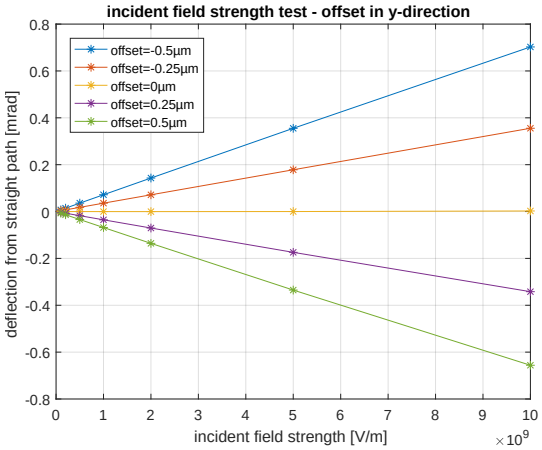

Figure 15: incident field strength test in y-direction

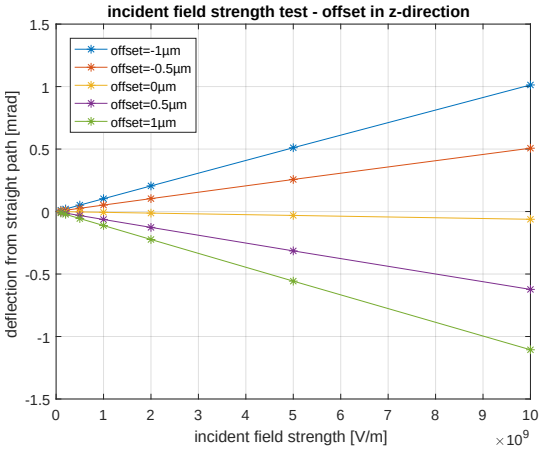

Figure 16: incident field strength test in z-direction

7 Optimisation results $3.3\mu m$

The wavelength of choice for the ACHIP experiment's laser is 2 μm [5] [6]. Though, as seen in section 14 fabrication of structures for such small wavelength is still a complex process. Therefore, increasing the wavelength might be necessary until fabrication processes are ready. According to research at Los Alamos National Laboratory (LANL) for dielectric acceleration a wavelength of 3.3 μm is considered the shortest periodicity of the structure at which the Nanoscribe is capable of producing reproducible structures. Therefore, as the refractive index for fused silica is about the same at 2 μm and 3.3 μm it was decided to do the simulations at the longer wavelength first. After all the simulations for a wavelength of 3.3 μm have been conducted, information on how the deflection results behave, if the refractive index stays approximately the same, but the wavelength and structure size get decreased will be crucial.

One of the main tasks of this thesis was to optimise the parameters of the focusing structure to receive the best deflection results. This was typically done by changing only one parameter at the time while keeping the others fixed to the previously optimised value. Different parameter dimensions were tested until a clear maximum was found or until the design prevented a further change of the parameter.

It should be noted that the parameter tests are not presented in the most logical way, but in the timeline they were tested. The initial dimensions of the parameters before the first test was conducted were chosen arbitrarily to be fractions or multiples of the wavelength. The dimensions were width $W = 825\,\text{nm}$, gap $G = 3.3\,\mu\text{m}$, height $H = 6.6\,\mu\text{m}$, curvature symmetric $C = 825\,\text{nm}$, shift $S = 0\,\text{nm}$, without the pillar head and simulated with 50 pairs of pillars.

As mentioned before, to each perfect phase point for a focusing field there is always a second phase point to achieve a defocusing field. All the following tests were done for both focusing and defocusing fields. To abstain from overloading this thesis with figures only the plots for the focusing field will be shown. A list of all plots created during this thesis is available on switchdrive [27]. The defocusing field plots are the same as the focusing plots mirrored at the y-axis and do not add any further insight.

As in an experiment the particles will hit the structure as bunches, the perfect phase will not be hit for all particles at the same time. Therefore, tests on how the deflection behaves if the particle hits the structure too early or too late were also done. These laser phase tests would add an even greater amount of figures to this thesis since they would have to be done for each dimension change of each parameter. Since the results of the laser phase tests do not drastically change with the parameter's dimension, they will once be presented in section 7.2 where the idea for them was explored and once at the end of the optimisation process to show the overall change.

7.1 pillar width test

The first test conducted was the pillar width test. In this case the tested values ranged from $W = 800\,\text{nm}$ up to $W = 1300\,\text{nm}$. As displayed in figure 17 and 18 there is a considerable difference in deflection at the greatest offsets. What can also be seen is that the curves in the z-direction tests do not hit the centre point. This will be seen in the z-direction plots of other parameters too and is caused by the asymmetry of the pillar leg.

In y-direction $W = 1200\,\text{nm}$ gives the strongest deflection. In z-direction the strongest deflection is caused by the 1100 nm case. Since there was no clear better results for one of those cases and since the deflection behaviour in y-direction due to the parallel effect was unexplainable, the decision for $W = 1100\,\text{nm}$ was made.

The optimal width has been chosen to $W = 1100\,\text{nm}$.

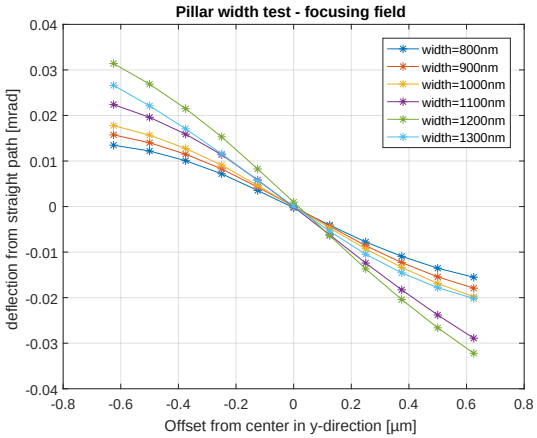

Figure 17: 3.3 μm pillar width test y-direction

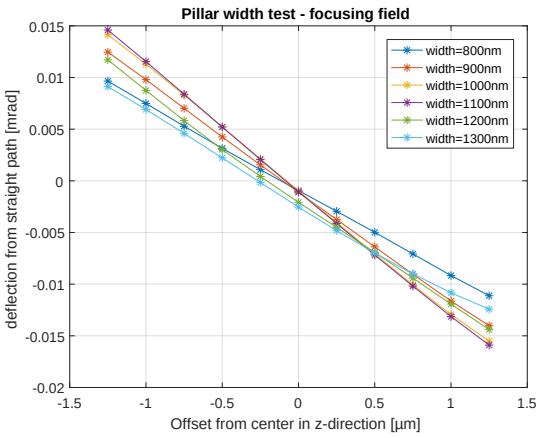

Figure 18: 3.3 μm pillar width test z-direction

7.2 symmetric curvature test

The second test focuses on the pillar's curvature and changed it symmetrically. The testes values ranged from $C = 500\,\text{nm}$ up to full pillars with $C = 1650\,\text{nm}$ were tested. Curvatures lower than $C = 500\,\text{nm}$ would have been possible too, but the stability of the pillars decreases with lower curvature values. As displayed in figure 19 and 20 only higher curvature values were plotted as they generally show stronger deflections. Though, not all the lower curvatures show less deflection than $C = 1100\,\text{nm}$ case, which is the weakest in this plots. Overall, there is another considerable difference in maximum deflection peaking at $C = 1400\,\text{nm}$ in both directions.

Since there was the concern that at higher curvatures means the results are less stable, i.e. arrival time variations for a particle has more difference on the deflection behaviour,

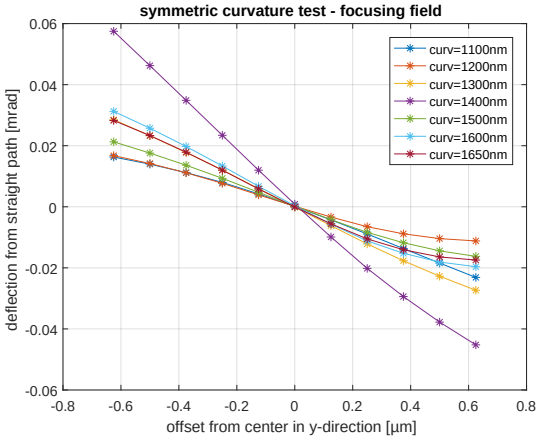

Figure 19: 3.3 μm symmetric curvature test y-direction

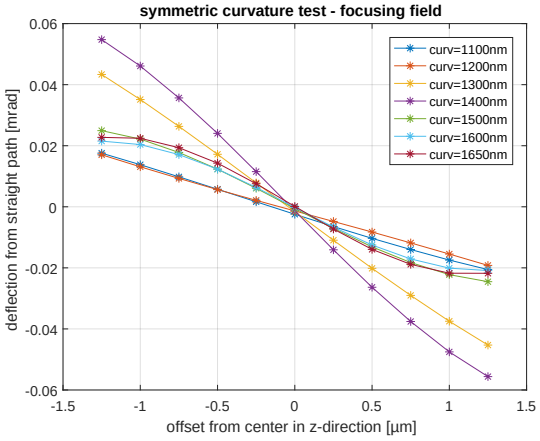

Figure 20: 3.3 μm symmetric curvature test z-direction

laser phase tests were done for both directions. The results of the laser phase tests in y-direction can be seen in figure 21, 22 and 23. The results for the z-direction test can be seen in figure 24, 25 and 26.

It can be clearly seen that the behaviours in y and z-direction strongly differ from each other. In z-direction there is mainly a change in slope. There is also a small shift of the curves especially at smaller curvatures, but that is due to the leg adding more asymmetry to the structure the smaller the curvature is. In y-direction the main difference between the curves is the so called parallel effect, which strongly shifts the curves up for late arrival and down for anticipated arrival. Though, it can be clearly seen that $C = 1400\,\text{nm}$ has less relative shift compared to its higher deflection than the plots with lower curvatures. Overall it is important to note that the results do not get less stable with higher curvatures. These findings helps fabrication process a lot since higher curvatures mean less overhang.

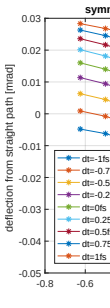

Figure 21: 3.3 μm curvature laser phase test y-direction 600 nm

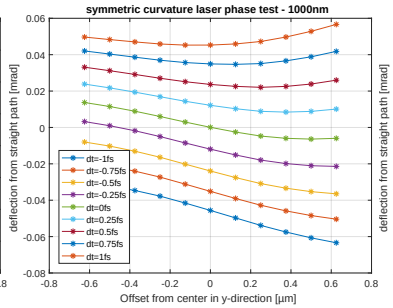

Figure 22: 3.3 μm curvature laser phase test y-direction 1000 nm

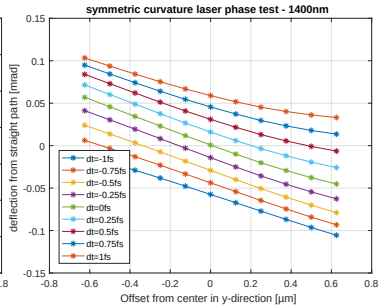

Figure 23: 3.3 μm curvature laser phase test y-direction 1400 nm

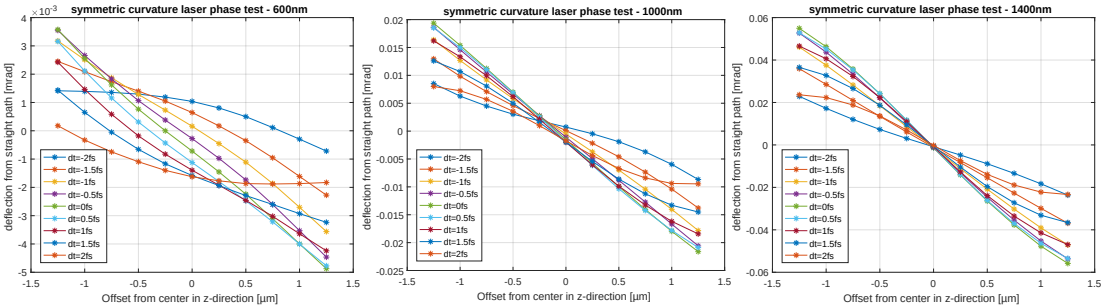

Figure 24: 3.3 μm curvature laser phase test z-direction 600 nm

Figure 25: 3.3 μm curvature laser phase test z-direction 1000 nm

Figure 26: 3.3 μm curvature laser phase test z-direction 1400 nm

The optimal symmetric curvature has been chosen to be $C = 1400\,\text{nm}$.

7.3 pillar gap test

The pillar gap test focuses on the gap between the front and the back pillars, which is measured from the inner side of the front pillar to the inner side of the back pillar. In this test fractions or slightly rounded fractions of the wavelength were tested. The dimensions ranged from $G = 1650\,\text{nm}$ up to $G = 3725\,\text{nm}$ or from $\lambda/2$ up to slightly more than $\frac{9}{8}\lambda$ as displayed in figure 27 and 28. It can be seen that in both cases the a gap of $\frac{3}{4}\lambda$ gives the best results. Also it has to be noted that $G = 2200\,\text{nm}$ was also tested since with $W = 1100\,\text{nm}$ a centre to centre pillar gap of exactly one wavelength is achieved. Though results show that this is not better than the 2475 nm case.

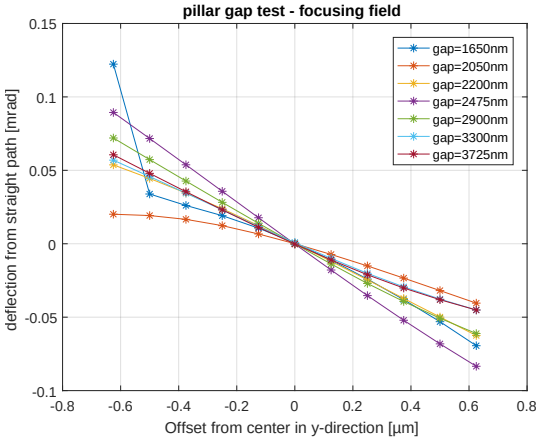

Figure 27: 3.3 μm pillar gap test y-direction

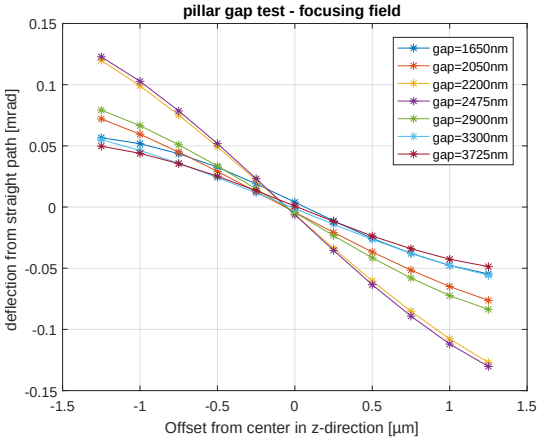

Figure 28: 3.3 μm pillar gap test z-direction

One further aspect of the y-direction plot is the sudden spike for an offset of $-0.625\,\mu$m for the smallest pillar gap of $\lambda/2$. This is caused by the fact that the particle is already

really close to the front pillar and the field does not seem to be linear up until this point. These spikes were seen in a greater extend in the 2 μm simulations as the offsets stayed the same, but the pillar gaps got even smaller. The reason why there is only a spike in negative offsets is probably explained by the fact that the deflection in y-direction hardly ever is completely symmetric with positive and negative offsets. The deflection is typically always stronger with negative offsets which might be explained by the fact that some parts of the amplitude are lost at the Bragg reflector. The alignment takes into account that the amplitudes of the laser and the Bragg reflector cancel each other out. If some parts of the amplitude are lost at the Bragg reflector to be able to cancel the laser at the alignment point, a different phase point of the Bragg's light has to hit the laser's light. The slope of the field at this different phase point is probably slightly smaller causing overall slightly weaker field amplitudes with positive offsets compared to negative ones.

The optimal pillar gap has been chosen to $G = 2475\,\text{nm}$.

7.4 pillar height test

The pillar height test focuses on the height of the pillars, which is measured from the substrate up to the highest point of the pillars. Once again fractions of the wavelengths were tested ranging from λ up to $\frac{5}{2}\lambda$ as displayed in figure 29 and 30. Since $H = 6600\,\text{nm}$ and $H = 7425\,\text{nm}$ resulted in pretty much an equal deflection, also $H = 7000\,\text{nm}$ and therefore slightly less than $\frac{17}{8}\lambda$ was tested. As expected from the first results, the overall deflection at $H = 7000\,\text{nm}$ was the highest.

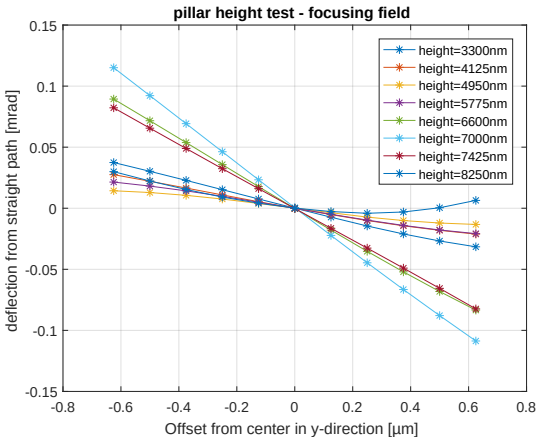

Figure 29: 3.3 μm pillar height test y-direction

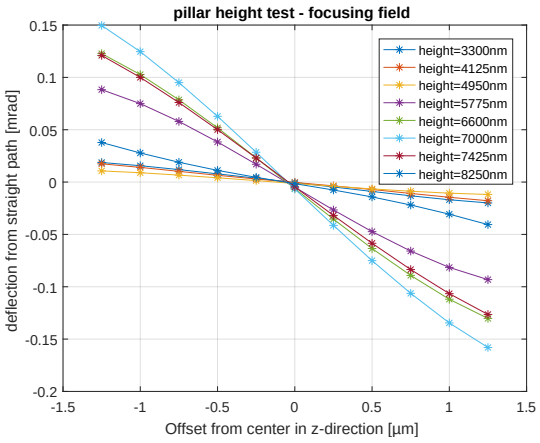

Figure 30: 3.3 μm pillar height test z-direction

As this test only consisted of changing the height and letting the curvature a and curvature b dimensions the same, the semi major axis of both ellipses gets stretched and therefore the curvature of the inner ellipse does not stay the same. One test that was

done was to stretch the curvature value according to the change in height. For example the dimension was stretched from $A = 1400\,\text{nm}$ to $A = 1500\,\text{nm}$ as the height was stretched from $H = 6600\,\text{nm}$ to $H = 7000\,\text{nm}$. Of course, a correct stretch would have been to stretch only the curvature a value to 1500 nm, but even this stretch in symmetric curvature already resulted in a higher deflection. Though, due to time constraints this was not further tested. At least it gives a little insight that the parameters are intertwined. To get the full extend of the structure it would be necessary also test such subtle changes. Another obvious examples of intertwined parameters could be the pillar width and the pillar gap as they both change in y-direction as height and curvature a both change in z-direction.

The optimal pillar height has been chosen to be $H = 7000\,\text{nm}$. Though, for comparability the parameters for the next tests remained the same as chosen after the pillar gap test.

7.5 curvature b test

The curvature b test focuses on the difference between the semi minor axes of the outer and inner ellipse. Since curvature a and curvature b were equally changed in the symmetric curvature test, a curvature a dimension of 1400 nm was chosen to make the tests comparable. The curvature b dimension ranged from thin 600 nm up to a full pillar of 1650 nm, where $B = 1400\,\text{nm}$ displays the same curve as the symmetric curvature one and is therefore the benchmark. The results are displayed in figure 31 and 32 and do not suggest a clear best case. While in z-direction a full pillar gives the best deflection, the best case in y-direction is between 1500 nm and 1600 nm.

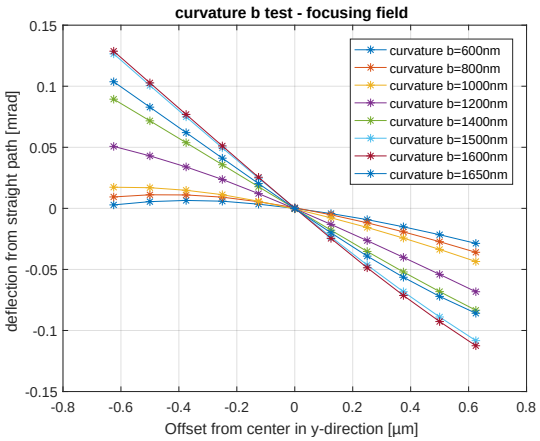

Figure 31: 3.3 μm curvature b test y-direction

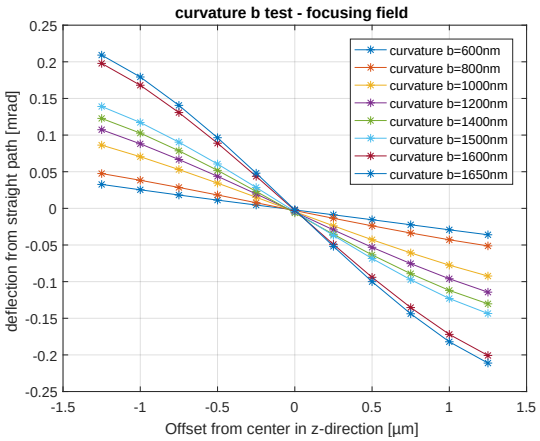

Figure 32: 3.3 μm curvature b test z-direction

The impact of a wrong laser phase was tested with every parameter, but most of the time the laser phase results did not change the decision on the best case. Though, for the curvature b dimension the laser phase test was the decisive factor. In z-direction the

laser phase results look as always. There is a symmetric decrease in slope the further the particle is from the perfect phase. Though, in y-direction apart from the parallel effect, the slopes changed drastically for the $B = 1600\,\text{nm}$ and $B = 1650\,\text{nm}$ case. This lead to nearly flat curves without any deflection regardless of the offset for the $-1\,\text{fs}$ case. Assuming that the change in slope would get stronger if optimisations continued with these cases, it was decided to continue optimisation with the $B = 1500\,\text{nm}$ case as it combines good deflection results with well behaved laser phase curves.

The optimal curvature b value has been chosen to be $B = 1500\,\text{nm}$.

7.6 curvature a test

The curvature b test focuses on the difference between the semi major axes of the outer and inner ellipse. Even though the curvature b test showed better results for slightly higher curvatures values, $B = 1400\,\text{nm}$ was chosen to make also this test comparable to the symmetric curvature test. The tested dimensions ranged from $A = 800\,\text{nm}$ up to a close to full pillar of $A = 3200\,\text{nm}$, where $A = 1400\,\text{nm}$ is the same case as the the optimised symmetric curvature and therefore the benchmark. Note that the curvature a parameter has twice the range as the curvature b or in the symmetric curvature case, which is limited by the b parameter. The results are displayed in figure 31 and 32 and show a clear best case for $A = 2400\,\text{nm}$. To have more accuracy $A = 2600\,\text{nm}$ was also tested, but showed results between $A = 2400\,\text{nm}$ and the $A = 2800\,\text{nm}$ case. Overall, especially in the z-direction test the deflections from $A = 2000\,\text{nm}$ up to $A = 3200\,\text{nm}$ lead to very similar results.

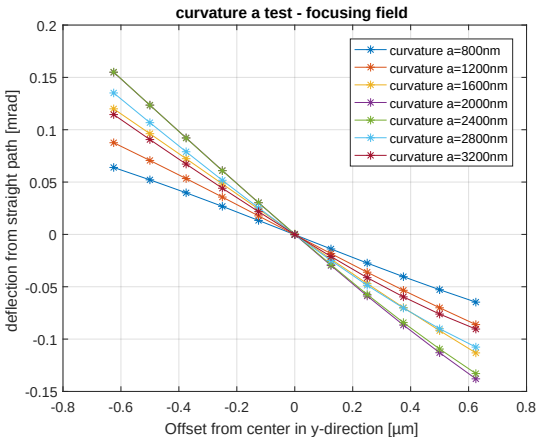

Figure 33: 3.3 μm curvature a test y-direction

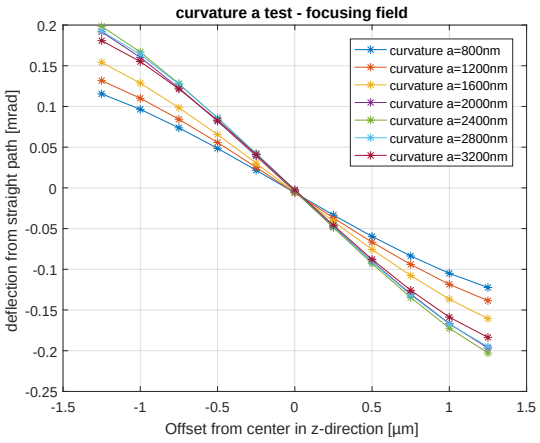

Figure 34: 3.3 μm curvature a test z-direction

The optimal curvature a dimension has been chosen to be $A = 2400\,\text{nm}$.

7.7 pillar shift test

In the pillar shift test the impact of the relative position between each pillar on the deflection performance is investigated. The initial case was a shift between the one front and one back pillar of half a wavelength. This results in the pillars perfectly aligned to each other as for example seen in figure **??**. A setup like this is called a shift of 0 nm. A full shift of half a wavelength means that the back pillar is completely hidden by the front pillar, which is called a shift of 1650 nm. This is the only test for a wavelength of 3.3 μm that was conducted with the pillar head present. Tested dimensions ranged from $S = 0$ nm up to $S = 1600$ nm were tested and are displayed in figure 35 and 36. As especially seen in the z-direction test, $S = 1400$ nm and $S = 1600$ nm show pretty much the same deflection, so $S = 1500$ nm was tested too, which resulted in even slightly higher deflection.

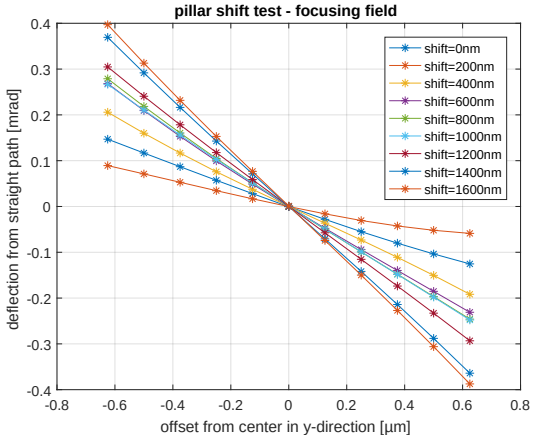

Figure 35: 3.3 μm pillar shift test y-direction

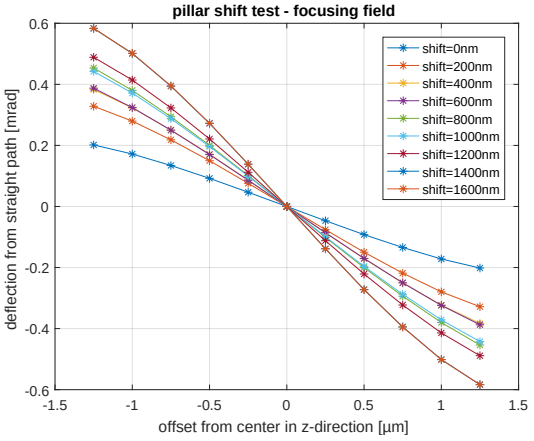

Figure 36: 3.3 μm pillar shift test z-direction

One remarkable result of this test was that not only the deflection increased drastically, but also the parallel effect shrank considerably. The change in slope for early or late particles increases once again, but not as severe as in section 7.5 and is easily overlooked by the strong shrinkage of the parallel effect.

The final dimensions taking into account all results are $W = 1100$ nm, $G = 2.475\,\mu$m, $H = 7\,\mu$m, $A = 2400$ nm, $B = 1500$ nm, $S = 1500$ nm using 50 pairs of pillars.

8 Optimisation results $2\mu m$

The aim of this section is to present the results obtained for a wavelength of 2 μm. Once again the tests are not presented in the most logical order, but in the order they were conducted, which is slightly different than in section 7 since some insight on the structure was already available. The initial dimensions were $W = 500\,\text{nm}$, $G = 2\,\mu\text{m}$, $H = 4\,\mu\text{m}$, $C = 500\,\text{nm}$, $S = 0\,\text{nm}$, without the pillar head and simulated with 50 pairs of pillars. It has to be noted that even though the amount of pillars is the same, there is still a difference in the deflection strength, as 50 pairs of pillars with a period of 2 μm mean a propagation distance of 100 μm, while in section 7 the propagation distance was 165 μm due to the 3.3 μm period. So, while not always perfect, the deflection results will be smaller by about a factor of 1.65.

8.1 pillar width test

Not only was the pillar width test with a wavelength of 2 μm the first test for 2 μm, but the first test in general since until that time it was not known how complex the fabrication will be. The dimensions ranged from 400 nm up to 800 nm, which, due to the smaller wavelength, is an even broader range than for the 3.3 μm equivalent test in section 7.1. The results are displayed in figure 37 and 38. The strongest deflection results are shown for about 600 nm.

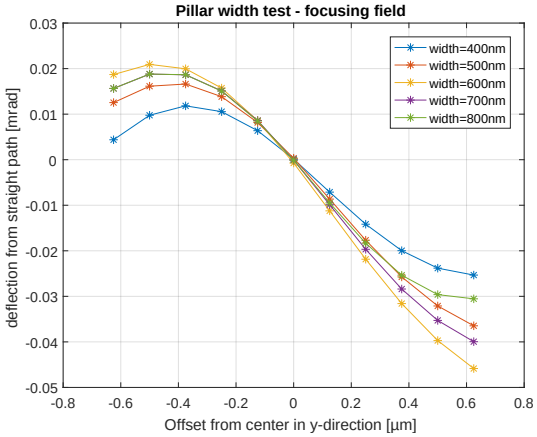

Figure 37: 2 μm pillar width test y-direction

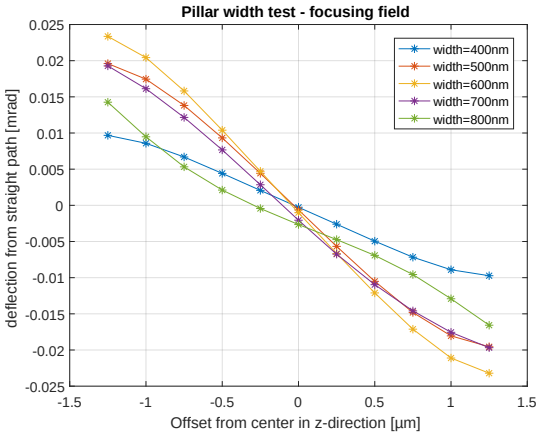

Figure 38: 2 μm pillar width test z-direction

From the 3.3 μm test in section 7.1 with an optimised width of $W = 1100\,\text{nm}$ one would expect the highest deflection at about $W = 666\,\text{nm}$, which is pretty close to these results. A difference to the 3.3 μm test is that the overall deflection in the 2 μm results is higher and are far less symmetric for positive and negative offsets. All of this might be explained by the lower propagation space as the results in section 11 show that a higher amount of pillars makes the results more uniform.

The optimal width has been chosen to be $W = 600\,\text{nm}$.

8.2 pillar gap test

The pillar gap test was conducted while the $3.3\,\mu\text{m}$ tests were still going on to try to get more insight on why 2475 nm shows the best results in the $3.3\,\mu\text{m}$ pillar gap test in section 7.3. Therefore, the head is still not present in this test. Though due to the fact that the symmetric curvature test for $3.3\,\mu\text{m}$ had already been conducted, a jump in parameters happened in this test. In the previous test the symmetric curvature was $C = 500\,\text{nm}$ while in this test the best symmetric curvature for a wavelength of $3.3\,\mu\text{m}$ was downscaled. Therefore, in this test $C = 850\,\text{nm}$. G ranged from $1250\,\text{nm}$ or $\frac{5}{8}\lambda$ up to $3000\,\text{nm}$ or $\frac{3}{2}\lambda$ and is displayed in figure 39 and 40. Notice that the maximum offset has been decreased starting from this test as the spikes present at larger offsets became prominent in pretty much each curve as the pillar gap dropped below one wavelength. The maximum offsets were now $-0.5\,\mu\text{m}$ up to $0.5\,\mu\text{m}$ in y-direction and $-1\,\mu\text{m}$ up to $1\,\mu\text{m}$ in z-direction. The decrease in z-direction would not have been necessary as the pillar gap does not influence the z-direction, but for comparison to the $3.3\,\mu\text{m}$ results in section 7 they were decreased accordingly.

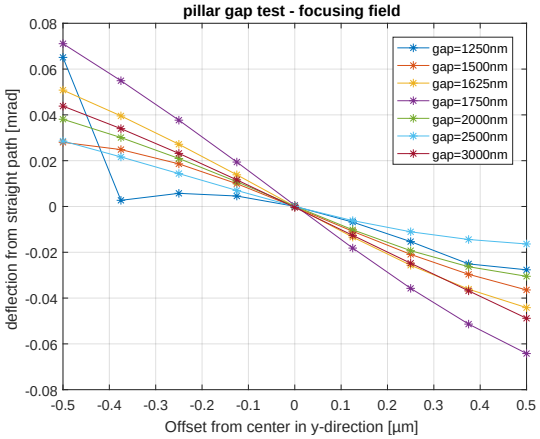

Figure 39: $2\,\mu\text{m}$ pillar gap test y-direction

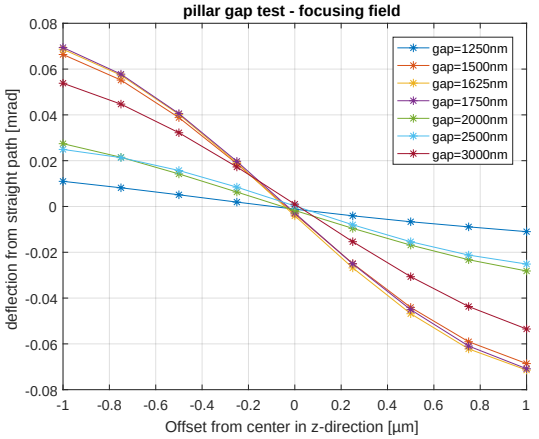

Figure 40: $2\,\mu\text{m}$ pillar gap test z-direction

The highest deflection is shown for a $G = 1750\,\text{nm}$, but especially in z-direction 1500 nm shows the same deflection. A quick test with $G = 1625\,\text{nm}$ was also done, because $G = 1500\,\text{nm}$ and $G = 1750\,\text{nm}$ are so close in z-direction. A gap of 1750 nm remains the best case. From the $3.3\,\mu\text{m}$ equivalent test in section 7.3 one would expect $G = 1500\,\text{nm}$ to be the best case. This indicates that it is not possible to scale perfectly with wavelength, but as $G = 2200\,\text{nm}$ in figure 28 gives pretty much the same results as $G = 2475\,\text{nm}$ one could expect a midpoint between $G = 2475\,\text{nm}$ and $G = 2900\,\text{nm}$ of about $G = 2675\,\text{nm}$ to also give similar deflection results as $G = 2475\,\text{nm}$ and $G = 2900\,\text{nm}$. In this hypothesis the scaling would work correctly. Overall, the scaling seems to work out pretty well. Though, some more extended tests would have to be

performed to get the full information about the structure's pillar gap behaviour.

The optimal pillar gap has been chosen to be $G = 1.75\,\mu$m.

8.3 symmetric curvature test

Starting from this test all other $2\,\mu$m tests have been conducted after all but the pillar shift test for $3.3\,\mu$m had been finished. Therefore, the pillar head, see figure 7, is present in all the following tests. The tested dimensions range from 500 nm up to a full pillar of 1000 nm. The results are displayed in figure 41 and 42. As the symmetric curvature in the previous test was already 850 nm, the increase in deflection is negligible as the highest deflection is given for a symmetric curvature of 900 nm.

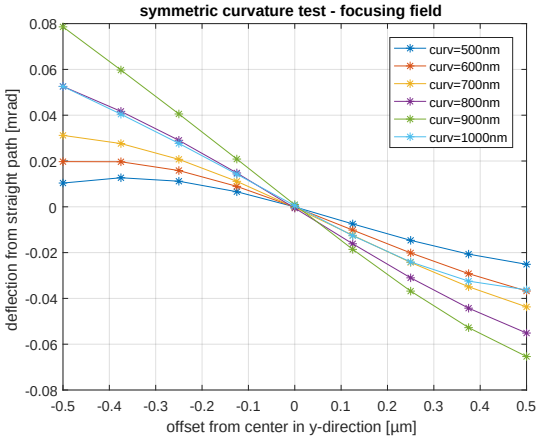

Figure 41: $2\,\mu$m symmetric curvature test y-direction

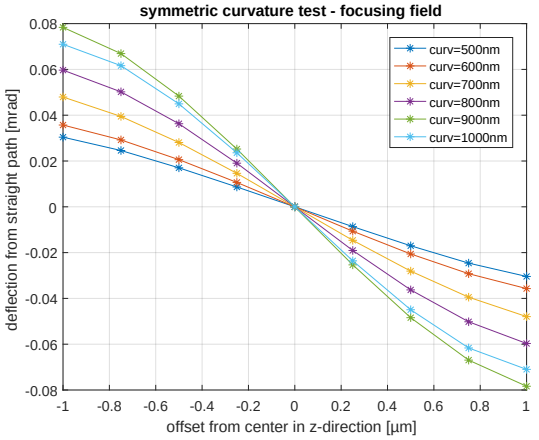

Figure 42: $2\,\mu$m symmetric curvature test z-direction

Since the curvature is limited and dominated by B, which had the highest deflection at 1500 nm at $3.3\,\mu$m the best curvature was expected to be 900 nm for a wavelength of $2\,\mu$m.

8.4 curvature b test

In this test, ca was kept at 900 nm and cb ranged from 500 nm up to 1000 nm. The results are displayed in figure 43 and 44. The highest deflection is observed for $cb = 900$ nm, which scales perfectly with the results of the $3.3\,\mu$m test in section 7.5. The results look extremely similar to the symmetric curvature results. The deflection seems to be dominated by cb even more than in the $3.3\,\mu$m case.
The optimal curvature b dimension has been chosen to be $cb = 900$ nm.

8.5 curvature a test

In this test, B was kept at 900 nm and the A ranged from 600 nm up to nearly a full pillar of 1800 nm. The results are displayed in figure 45 and 46. It can be clearly seen

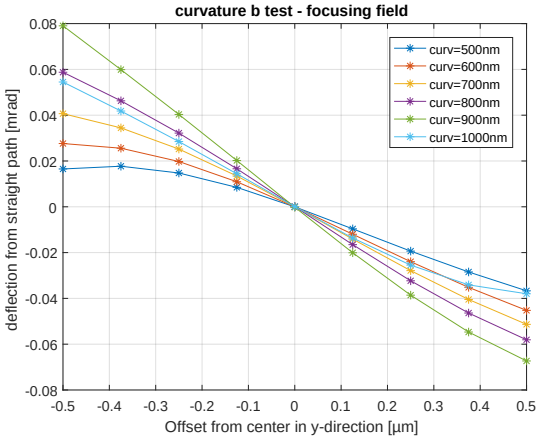

Figure 43: $2\,\mu$m curvature b test y-direction

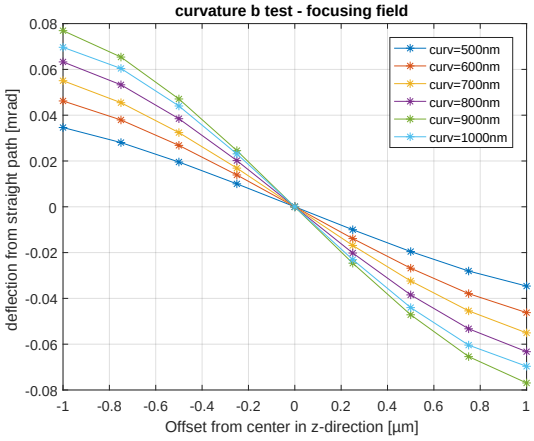

Figure 44: $2\,\mu$m curvature b test z-direction

why the curvature b results did not differ much from the symmetric curvature ones as there is hardly any change with *ca*. This was also the case for a big range in the equivalent $3.3\,\mu$m curvature a test in section 7.6. Therefore, the best value for A cannot be decided as the curves are too close in z-direction and in y-direction the deflection slightly increases with lower curvatures.

Overall scaling works pretty fine also with this test, even though there is a little mismatch in the curvature a results, which is not that severe as the deflections do not change drastically. Also the observation could be different if in the $3.3\,\mu$m curvature a test (in section 7.6) $B = 1500\,\text{nm}$ would have been chosen instead of $B = 1400\,\text{nm}$.

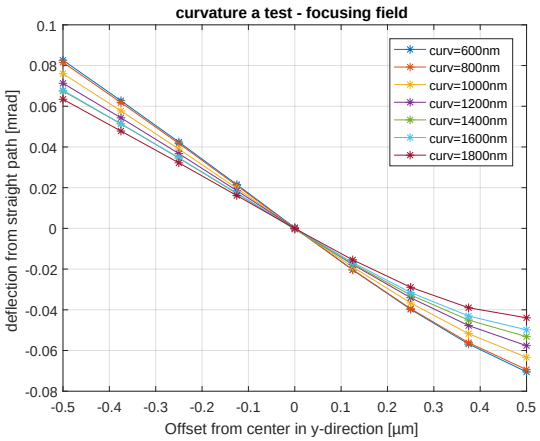

Figure 45: $2\,\mu$m curvature a test y-direction

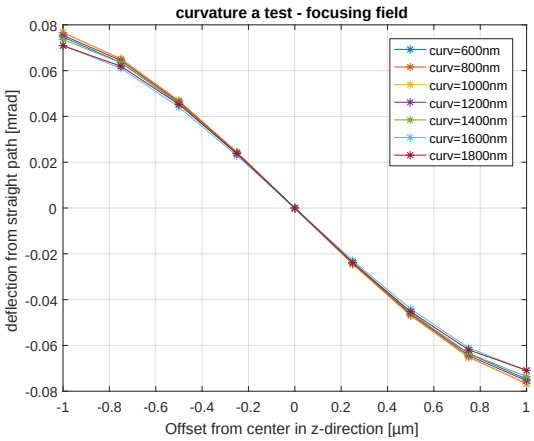

Figure 46: $2\,\mu$m curvature a test z-direction

As no best case was chosen, the results from the symmetric curvature test were reused

for the further tests.

8.6 pillar height test

H ranged from 3500 nm up to 4500 nm and was therefore not as broad as in the equivalent 3.3 μm pillar height test in section 7.4. The expectation was to find the highest deflection at about $\frac{17}{8}\lambda$ or about 4250 nm. The results are displayed in figure 47 and 48. Especially in z-direction the highest deflection was found for the expected value H, while in y-direction the deflection for the 4000 nm and 4250 nm are about the same. Scaling wise this is one of the best tests. An explanation why a pillar height of slightly higher than two times the wavelength gives the best results is still not known.

Even thought slightly higher pillars result in better deflection, the dimensions for the further tests were kept unchanged.

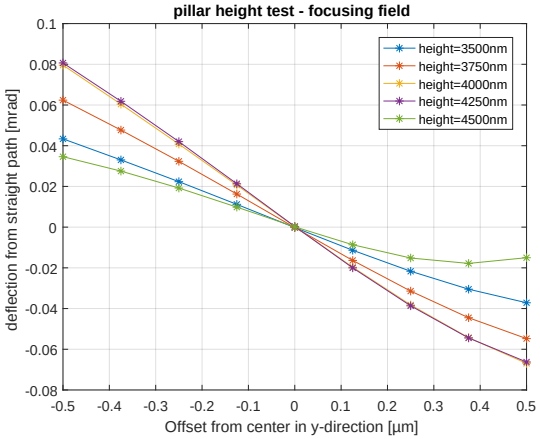

Figure 47: 2 μm pillar height test y-direction

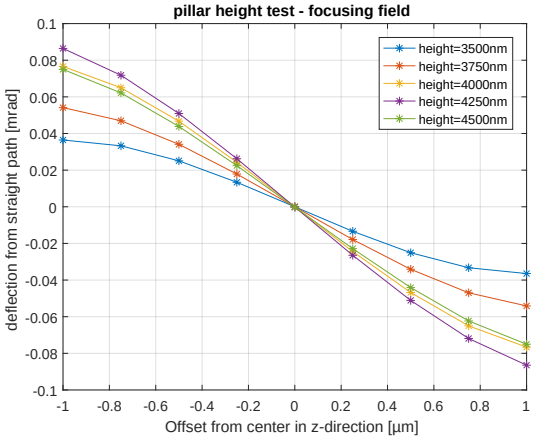

Figure 48: 2 μm pillar height test z-direction

8.7 pillar shift test

The values ranged from $S = 0$ nm to a nearly full shift of $S = 1000$ nm. As seen in figure 49 and 50, not all shifts are displayed to make the figures less cramped. The best result is achieved for$S = 700$ nm. This is the worst scaling so far as a shift between 850 nm and 1000 nm was expected from the results of the 3.3 μm tests in section 7.7. A clear reason why the scaling does not work perfectly in this case could not be found. The general behaviour is the same as there is a slight decrease in deflection at about one third of the maximum shift. In the 3.3 μm pillar shift test there is another slight decrease in deflection at about two thirds of the maximum shift. In the 2 μm case the overall maximum is instead observed there.
Also in this test not only did the maximum deflection increase, but also the parallel effect strongly decrease. The magnitude of the parallel effect is about the same as in the

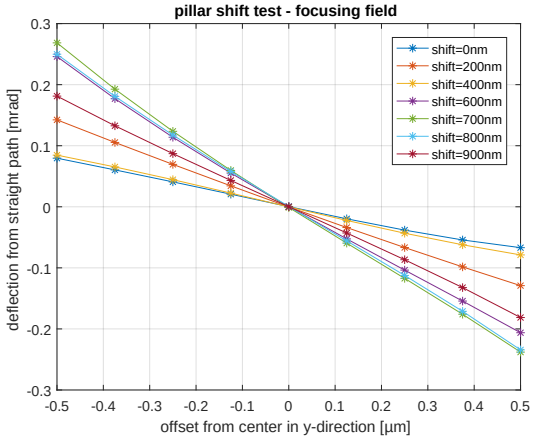

Figure 49: 2 μm pillar shift test y-direction

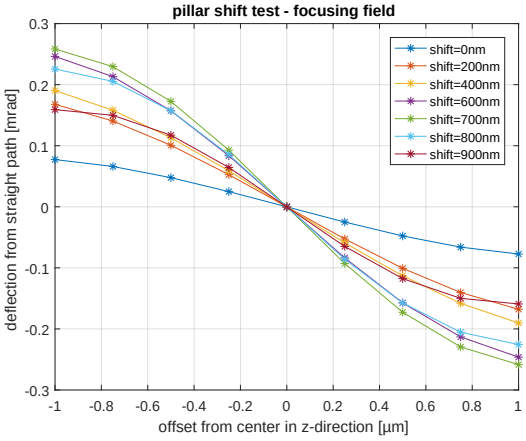

Figure 50: 2 μm pillar shift test z-direction

3.3 μm case and the change in slope even more symmetric.

The final dimensions taking into account all results are width $W = 600\,\text{nm}$, gap $G = 1.75\,\mu\text{m}$, height $H = 4.25\,\mu\text{m}$, curvature symmetric $C = 900\,\text{nm}$, shift $S = 700\,\text{nm}$, with the pillar head and were simulated using 50 pairs of pillars.

9 refractive index

The ACHIP experiment [5, 6] is not focused on one specific material. Therefore, it is necessary to test different materials to find the one with the best behaviour. So, apart from knowing how to scale the dimensions of the parameter, if the wavelength is changed, it is also crucial to know the behaviour of the structure, if the refractive index is changed.

To test the impact of a change in the refractive index, it has been varied as a parameter. The tested indices were the $n = 1.6$, $n = 1.8$ and $n = 2$. The results were compared to the curves of the actual refractive index. Once again this was done both using a wavelength of $3.3\,\mu$m and $2\,\mu$m. Also, there are two ways to evaluate the refractive index. The first test is to keep all parameter dimensions unchanged and just change the refractive index and the second way is to decrease the width of the material according to the refractive index to keep the same phase shift within the material. In both cases the meshing accuracy has been increased to account for the lower wavelength within the material to keep the same overall accuracy.

9.1 refractive index test $3.3\mu m$

The refractive index tests for a wavelength of $3.3\,\mu$m were one of the first tests conducted and therefore used the dimensions of the pillar width test with $W = 1100\,$nm, $G = 3.3\,\mu$m, $H = 6.6\,\mu$m, $C = 825\,$nm, $S = 0\,$nm, without the pillar head and were simulated using 50 pairs of pillars.

The results for the tests which kept every parameter dimension the same are displayed in figure 51 and 52.

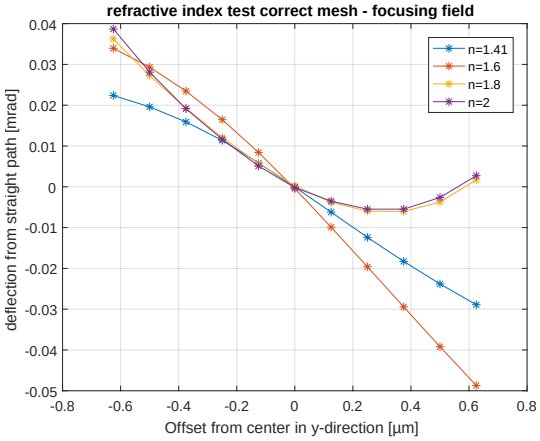

Figure 51: $3.3\,\mu$m refractive index test y-direction

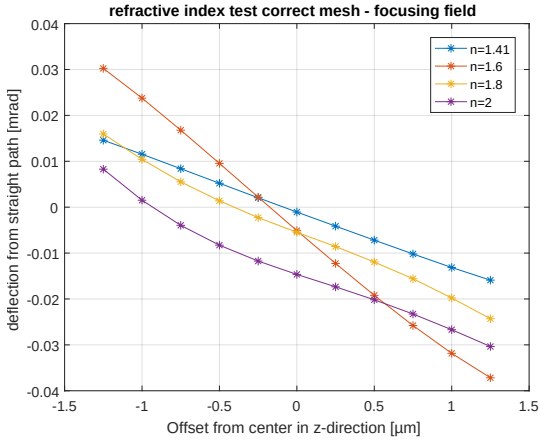

Figure 52: $3.3\,\mu$m refractive index test z-direction

The parallel effect in z-direction is caused by the leg and is strongly increased due to the higher refractive index. This makes sense as there is a stronger asymmetry between

the upper and the lower part of the structure. The behaviour of the deflection changes significantly in z-direction. In y-direction higher refractive indices show far worse results.

In the second test the width of the pillars was adapted to have the same phase shift in the material. The width for different refractive indices were calculated like

$$d = d_0 \frac{n_0}{n} \tag{8}$$

where $d0 = 1100\,\text{nm}$, $n0 = 1.43$ and rounded. The calculated width for $n = 1.6$, $n = 1.8$ and $n = 2$ were $d = 969nm$, $d = 861nm$ and $d = 775nm$. Therefore $W = 1000nm$, $W = 900nm$ and $W = 800nm$ were used. The results for these tests are displayed in figure 53 and 54.

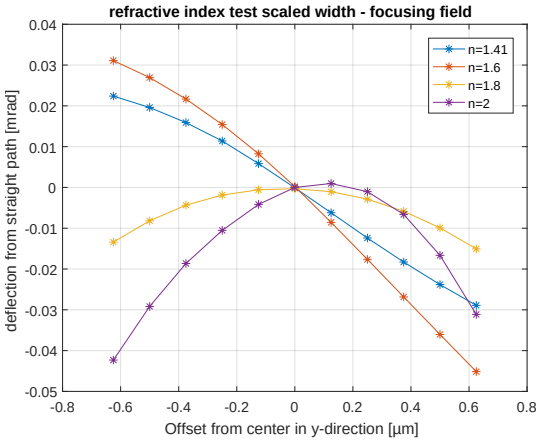

Figure 53: 3.3 μm refractive index test y-direction with scaled width

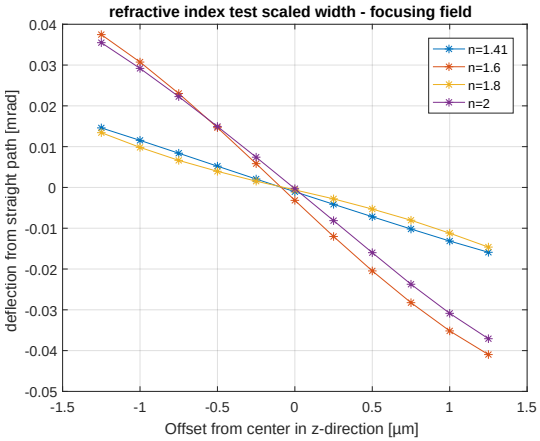

Figure 54: 3.3 μm refractive index test z-direction scaled width

The parallel effect in z-direction is minimised and actually shows quite good results. In y-direction, instead, the results are even worse. While they hardly change for a refractive index of $n = 1.6$, higher indices show neither focusing nor defocusing results. This means that the whole optimisation for a wavelength of 3.3 μm should be repeated, if the wavelength changes.

9.2 refractive index test $2\mu m$

The refractive index tests for a wavelength of 2 μm were performed after all parameters but the pillar shift were tested. Therefore the dimensions of the parameters were $W = 600nm$, $G = 1.75\mu m$, $H = 4000\mu m$, $C = 900nm$, $S = 0nm$, with the pillar head and were simulated using 50 pairs of pillars.

The results for the tests which kept every parameter dimension the same are displayed in figure 55 and 56 and show a similar picture as the 3.3 μm results. While the results in

z-direction look quite good even though the slope changes drastically with refractive indices, the results in y-direction are extremely asymmetric and show no linear dependency at all.

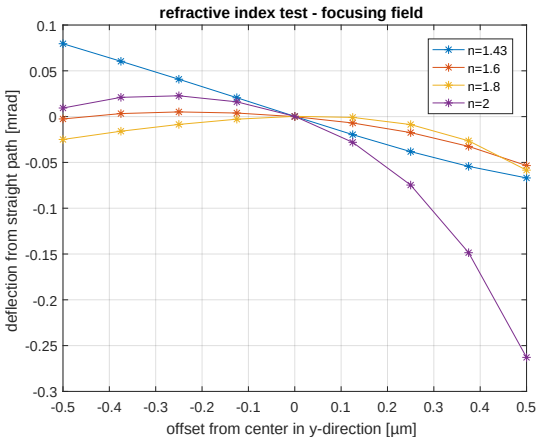

Figure 55: 2 μm refractive index test y-direction

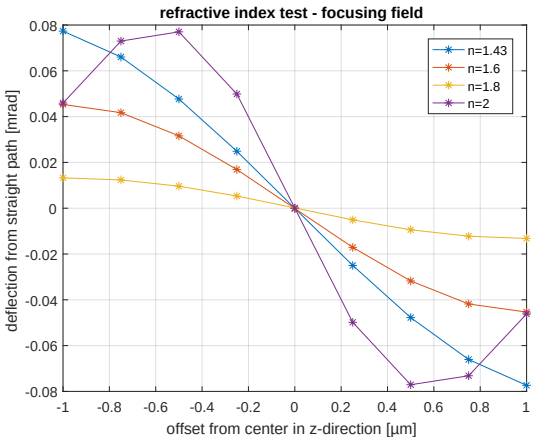

Figure 56: 2 μm refractive index test z-direction

For the scaled width test, the calculated width for $n = 1.6$, $n = 1.8$ and $n = 2$ were $d = 536nm$, $d = 476nm$ and $d = 429nm$. Here no structures with corresponding similar width were available. Therefore, $W = 540nm$, $W = 480nm$ and $W = 430nm$ were designed and simulated. The results for these tests are displayed in figure 57 and 58

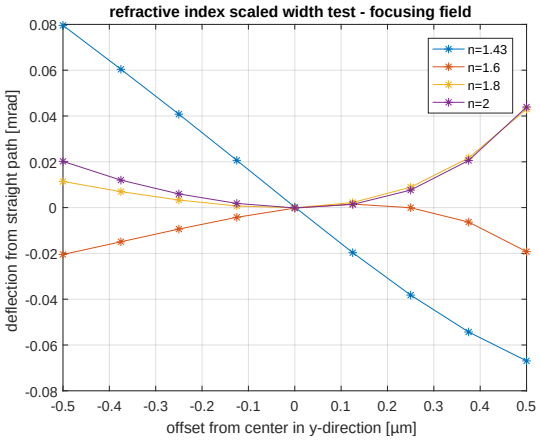

Figure 57: 2 μm refractive index test y-direction with scaled width

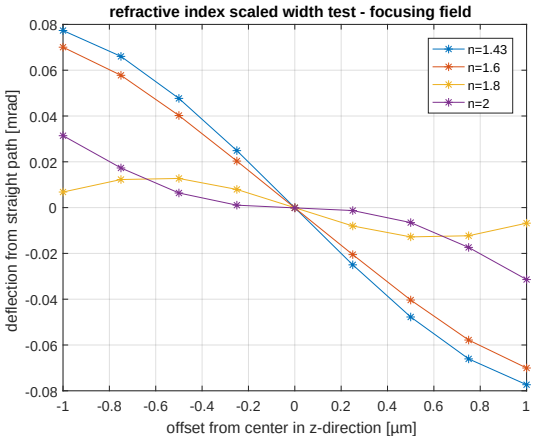

Figure 58: 2 μm refractive index test z-direction scaled width

and again show similar results to the 3.3 μm results in z-direction, but are severely different from the initial $n = 1.43$ simulation.

Overall these results for both wavelengths are not promising at all. The 3.3 μm re-

sults with an extra pillar head should give scalable curves at least in z-direction. In y-direction the pillar widths does not seem to be the only crucial parameter. The fact that the results generally look worse in the $2\,\mu$m simulations might be better understood if one observes that the pillars are nearly full. Therefore, a higher refractive index changes the phase of the laser for the whole illumination area. In the $3.3\,\mu$m case the curvature dimension was exactly half the of the wavelength. So, half of the illumination area let the laser's light pass without changing its phase.

Future simulations should focus on the parameter dimension's changes in case the material is changed. As especially the plots in y-direction are affected by the change in refractive index, the pillar gap might be crucial as it is the only other parameter along the y-direction. As mentioned before, also the curvatures might be important as bigger parts of the recording volume are affected by the changes. If none of the parameters seems to solve the issues, a sensitivity study on the refractive index should be considered.

10 mathematical description of the deflection

To have a better understanding of the deflection behaviour of the structure, some time was invested trying to set up a mathematical model replicating the deflection strength and the effects seen in the simulation results, namely the parallel effect and the change in slope. Of course not all curves will be described perfectly and this is not a substitute for simulations as getting the field data used to describe the effects need the simulation results. Therefore, this description is a mathematical model of the particle tracking to gains some information on which parts of the fields have to be optimised to get the desired results.

The particle's behaviour in the simulation volume is described by the Lorentz force, which consists of three equations

$$\begin{aligned} F_x &= -e_0 \cdot (E_x + v_y B_z - v_z B_y) \\ F_y &= -e_0 \cdot (E_y - v_x B_z + v_z B_x) \\ F_z &= -e_0 \cdot (E_z + v_x B_y - v_y B_x) \end{aligned} \tag{9}$$

for the three spatial components. Hitting the perfect phase, the particle is deflected as seen in the offset test plots. To describe the behaviour in y or z-direction if a particle reaches the pillars too early or to late, only the latter two seem to be important for the deflection, but the effect the force in x-direction has on the velocity of the particle should not be ignored, in particular for slower particles. Though, as not all components of the electric and magnetic field have the same intensity and depend on the particular direction of the offset, this description will be split up into two parts, one for each of the offset directions.

This mathematical description will focus on recreating the deflection behaviour displayed in section 8.3 for a symmetric curvature of 900 nm as this case combines high deflection results with really well situated perfect phase points in y and z-direction. This approach is completely general if the appropriate electric and magnetic field is used.

10.1 deflection behaviour with offset in z-direction

First it is important to look at the fields the particle interacts with on its way through the pillars. Figure 59 displays the average fields the particle experience at different offsets and time differences from the perfect phase. A perfect phase was once again the phase with the highest deflection. In this case none of the field components is considerably smaller than the others. Therefore, none of the field components should be discarded. As these simulations were performed for ultra-relativistic particles and considering that the highest deflection seen in the simulations are lower than 1 mrad, the terms in the equations, where a velocity in y or one in z-direction couples to one component of the magnetic field, can therefore be discarded.

In this approximation equation 9 becomes

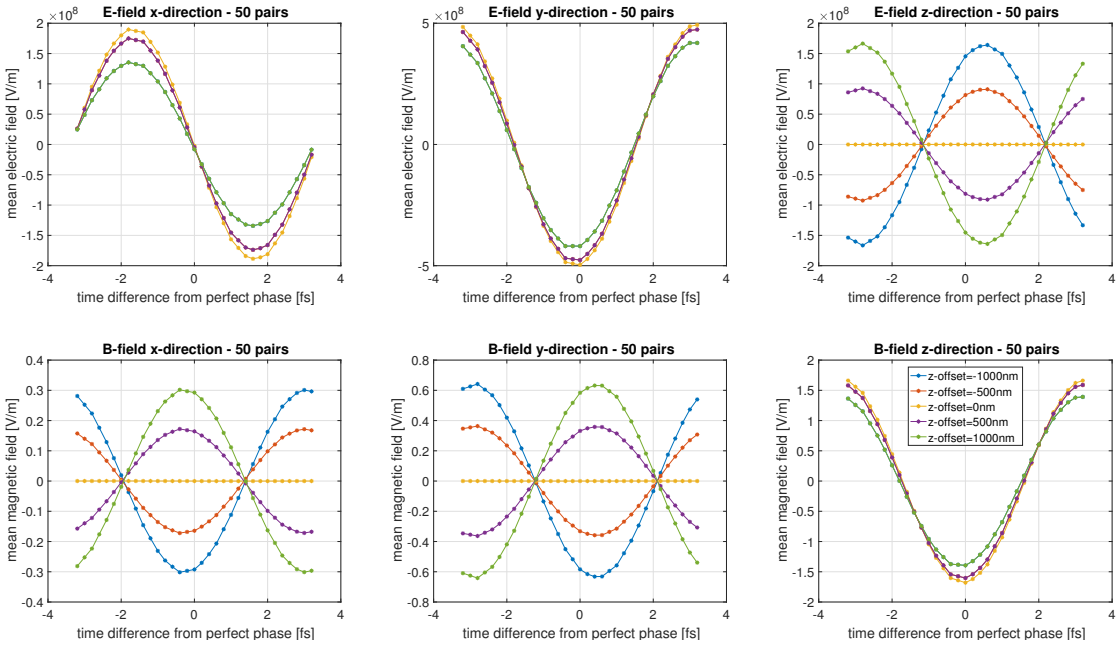

Figure 59: mean fields at perfect phase for focusing z-direction

$$\begin{aligned} F_x &= -e_0 \cdot (E_x) \\ F_y &= -e_0 \cdot (E_y - v_x B_z) \\ F_z &= -e_0 \cdot (E_z + v_x B_y). \end{aligned} \tag{10}$$

In Simulations it was observed that switching off the electric field in x-direction has no effects on neither the deflection results nor the mean fields of the other components. E_x hardly changes v_x. Therefore, the term $v_x B_z$ can be discarded in the second equation. Of course, ignoring field components is not physical as Maxwell's equations are not satisfied anymore. Though, as their impact is small, the terms can be put to zero.

10.1.1 effects of the force in z-direction

As the change in slope in the z-deflection plots is the least complicated effect, it was decided to start with it. As seen in figure 59 the electric field in z-direction and the magnetic field in y-direction show the same behaviour. The phase dependence of the two curves can be described by an offset dependent amplitude and a cosine

$$\begin{aligned} E_z &= E_\Delta \cdot cos(\Phi) \\ B_y &= B_\Delta \cdot cos(\Phi). \end{aligned} \tag{11}$$

where E_Δ and B_Δ are the amplitudes of the curves seen in figure 59 at zero offset. The offset dependence of the two curves is opposite. While the amplitude of the magnetic

field in y-direction increases for positive offsets, it decreases for the electric field in z-direction. As the amplitude at zero offset is negligible compared to the amplitudes with offsets, the offset dependence of the amplitude can be described linearly by its offset with different signs for the electric and magnetic field

$$\begin{aligned} E_\Delta &= -A_{zz} \cdot \Delta \\ B_\Delta &= +M_{zz} \cdot \Delta. \end{aligned} \tag{12}$$

where A_{zz} and M_{zz} are the slopes of the amplitude change seen in figure 59 and Δ is the offset. The Lorentz force in z-direction can be rewritten as

$$F_z = -e_0 \Delta \cdot (-A_{zz} \cdot cos(\Phi) + v_x M_{zz} \cdot cos(\Phi)) \tag{13}$$

where A_{zz} is the change in amplitude with offset for the electric field and M_{zz} is the change in amplitude with offset for the magnetic field. The equation can be further simplified by expanding the cosine according to Taylor for small angles.

$$cos(\Phi) = \left(1 - \frac{\Phi^2}{2} + O(\Phi^4)\right) \tag{14}$$

stopping at the quadratic term. According to the equation positive and negative changes in the phase decrease the electric field strength equally. Though, this behaviour is not always perfectly seen in the results. One effect that is easily overlooked, but equally important, is the shift at times different of 0 fs. If those shifts are equal, the assumption of expanding the curves at 0° is still correct as it just changes the maximum value, but the slope of the description will be the same for both curves. In the simulation results, the shift is not the same. It is hardly visible, but the maximum of the electric field in z-direction is shifted slightly more positive than for the magnetic field in y-direction. The actual angles to be inserted into the equation therefore have to be subtracted by the shifts.

Inserting the values for the change in amplitude $A_{zz} = 1.64 \times 10^{14}\,\mathrm{V/m^2}$ and $M_{zz} = 0.63 \times 10^{6}\,\mathrm{Vs/m^3}$ and the phase shifts $\Phi_{Ezz} = 0.47\,\mathrm{rad}$ and $\Phi_{Bzz} = 0.377\,\mathrm{rad}$ fitted from figure 59 into the equation

$$F_z \approx -e_0 \Delta \cdot \left(-A_{zz} \cdot \left(1 - \frac{(\Phi - \Phi_{Ezz})^2}{2}\right) + v_x M_{zz} \cdot \left(1 - \frac{(\Phi - \Phi_{Bzz})^2}{2}\right)\right) \tag{15}$$

and plotting the angle using

$$\alpha_{zz} = \frac{v_z}{v_x} = \frac{a_z T}{v_x} = \frac{F_z T}{\gamma m_0 v_x} \tag{16}$$

where $T = 3.33 \times 10^{-13}\,\mathrm{m\,s^{-1}}$ is the time it takes the particle to propagate through 50 pairs of pillars with a wavelength of $2\,\mu$m, $\gamma \approx 70.71$ is the Lorentz factor and $m_0 = 9.1 \times 10^{-31}\,\mathrm{kg}$ is the mass of the electron results in the curves displayed in figure 60.

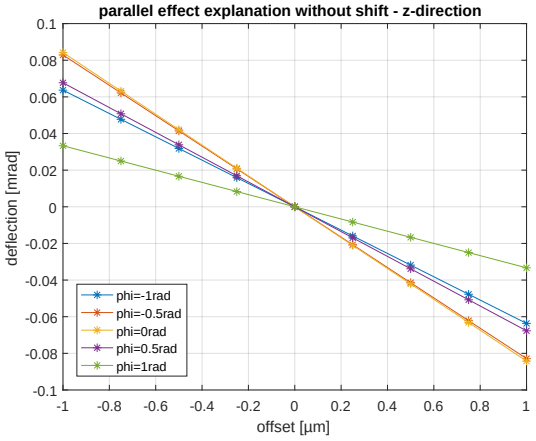

Figure 60: deflection with z-offset in z-direction with shift

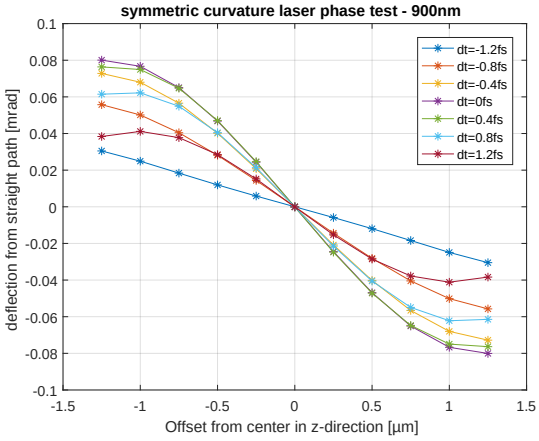

Figure 61: 2 μm symmetric curvature laser phase test z-direction

For comparison figure 61 shows the laser phase test in z-direction for a symmetric curvature dimension of 900 nm. An angle of

$$1\,\text{rad} = 57.3^\circ = 1.06\,\text{fs} \tag{17}$$

using a wavelength of 2 μm and therefore 6.66 fs is therefore similar to the laser phase test's delays. Of course the description is not perfect and could be improved, for example by defining a phase shift which varies with offset or even phase. Also the linear offset dependence is an assumption and could be improved. Overall the deflection results are well reproduced and especially the positive phase differences show pretty similar slope changes.

For the mathematical description a possible optimisation of the structure has to deal with obtaining the same phase shift for the electric and magnetic fields.

10.1.2 effects of the force in y-direction

As it can be seen in figure 59 the electric field in y-direction and the magnetic field in z-direction both are not negligible, so the effects of a z-offset on deflection in y-direction can be studied. The effects were observed before, but as they generally were small compared to the overall deflection, they were not studied that thoroughly until the end of the optimisation process.

Once again the curves can be described by a cosine. Though this time the behaviour with offset is different. First the change in amplitude is symmetric in offsets. The amplitude decreases symmetrically as the offset increases. The amplitude rate is different from before. So in this case there is an offset dependence in the amplitude change. This change is not linear and can be described as

$$E_\Delta = E_{zy0} + A_{zy} \cdot \frac{|\Delta|^2}{\Delta_0}$$
$$B_\Delta = B_{zy0} + M_{zy} \cdot \frac{|\Delta|^2}{\Delta_0} \tag{18}$$

where E_{zy0} and B_{zy0} are the amplitudes, A_{zy} and M_{zy} are the slopes of the amplitude change and $\Delta_0 = 250\,\text{nm}$. Δ_0 was chosen to fit the offset's step size in figure 59. Therefore, at for example an offset of 1000 nm the slope of the amplitude change is 4 times as strong. The change in amplitude are therefore calculated using the difference between the curve for zero offset and the one with 250 nm offset.

Again inserting the values for the amplitudes $E_{zy0} = -4.97 \times 10^8\,\text{V m}^{-1}$ and $B_{zy0} = -1.674\,\text{Vs/m}^2$, the change in amplitude $A_{zy} = 2 \times 10^{13}\,\text{V/m}^2$ and $M_{zy} = 8 \times 10^4\,\text{Vs/m}^3$ and the phase shifts $\Phi_{Ezy} = 0.118\,\text{rad}$ and $\Phi_{Bzy} = 0.047\,\text{rad}$ taken from figure 59 into the equation

$$F_y = -e_0 \cdot \left[\left(E_{zy0} + A_{zy} \cdot \frac{|\Delta|^2}{\Delta_0} \right) \cdot \left(1 - \frac{(\Phi + \Phi_{Ezy})^2}{2} \right) \right]$$
$$+e_0 \cdot \left[\left(B_{zy0} + M_{zy} \cdot \frac{|\Delta|^2}{\Delta_0} \right) \cdot \left(1 - \frac{(\Phi + \Phi_{Bzy})^2}{2} \right) \right] v_x \tag{19}$$

and plotting the angle calculated using the force in y-direction results in the curves displayed in figure 65.

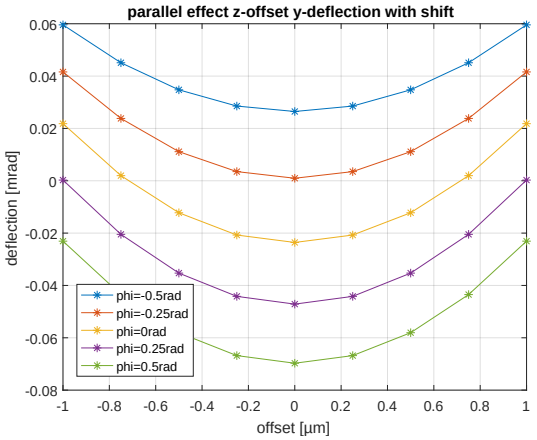

Figure 62: deflection with z-offset in y-direction with shift

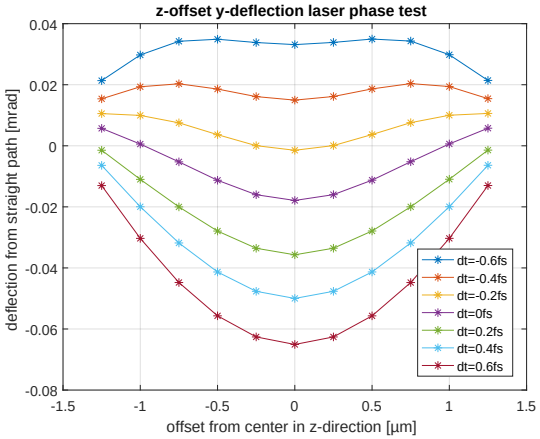

Figure 63: 2 μm symmetric curvature z-offset y-deflection laser phase test

For comparison figure 63 shows the laser phase test of the y-deflection with an offset in z-direction for a symmetric curvature dimension of 900 nm. It can be clearly seen that

the mathematical model is not able to fully describe the behaviour at especially high offsets and high phase changes. The differences concerning the offset might be described by the fact that the change amplitude does not linearly increase with offset. Using the mathematical model would result in $A_{zy} = 8 \times 10^{13}\,\mathrm{V/m^2}$ for an offset of 1000 nm, while looking at the data the actual change in amplitude is closer to $A_{zy} = 7 \times 10^{13}\,\mathrm{V/m^2}$. Depending the phase dependency there also is a difference in the shifts of the maxima with changing offsets, which also was not accounted for in this mathematical model.

Especially the perfect phase at zero offset is really similar to the simulation results, but also the general behaviour of the curves with zero offset is close to the simulation results. Further simulations will have to try to find a setup, where the shifts in maxima are the same to minimise the parallel effect. Keeping the shift in maxima as constant as possible with changing offsets will decrease the change in curvature at higher offsets.

10.2 deflection behaviour with offset in y-direction

The same ideas can be applied for offsets in y-direction. The mean fields are displayed in figure 64 and are differently than the ones for offsets in z-direction.

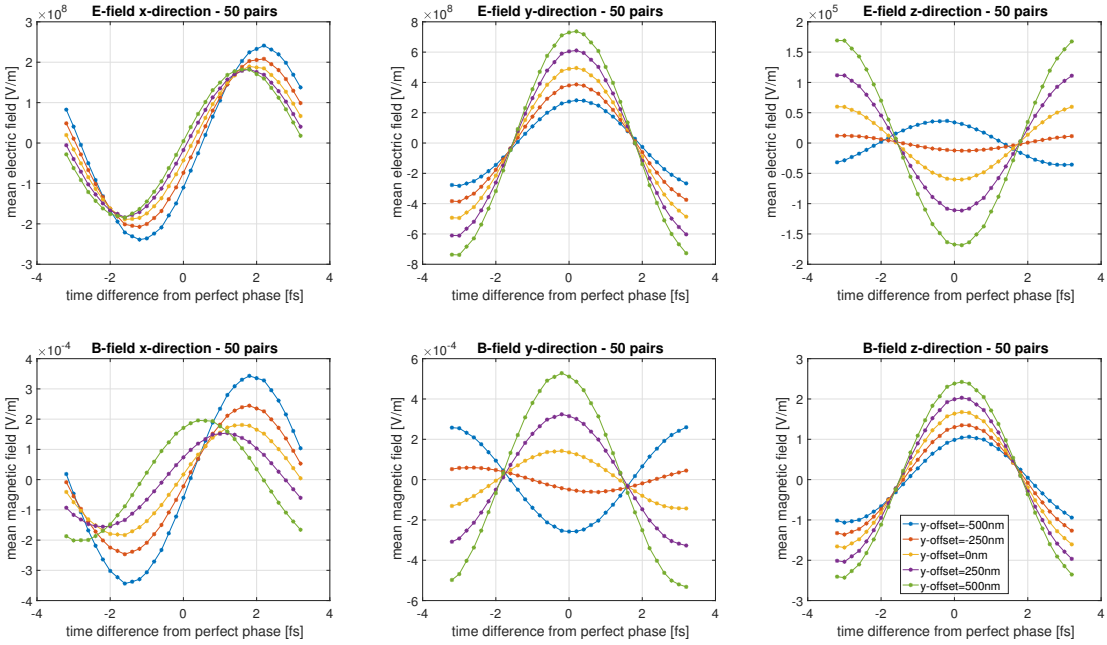

Figure 64: mean fields at perfect phase for focusing y-direction

In this case the electric field in z-direction and the magnetic field in y-direction are smaller by more than a factor 1000. Therefore, the force in z-direction at offsets in y-direction is negligible and can therefore be discarded. The description of the force in y-direction is similar to section 10.1. Both the amplitude of the electric and the magnetic field are described by a cosine with linear dependence on the offset

$$\begin{aligned} E_\Delta &= E_{yy0} + A_{yy} \cdot \Delta \\ B_\Delta &= B_{yy0} + M_{yy} \cdot \Delta. \end{aligned} \tag{20}$$

where the parameters are defined as in section 10.1.2. Inserting the values for the amplitudes $E_{yy0} = 4.97 \times 10^8\,\mathrm{V\,m^{-1}}$ and $B_{yy0} = 1.678\,\mathrm{Vs/m^2}$, the change in amplitude $A_{yy} = 4.83 \times 10^{14}\,\mathrm{V/m^2}$ and $M_{yy} = 1.5 \times 10^6\,\mathrm{Vs/m^3}$ and the phase shifts $\Phi_{Eyy} = 0.118\,\mathrm{rad}$ and $\Phi_{Byy} = 0.2\,\mathrm{rad}$ taken from figure 64 into the equation

$$\begin{aligned} F_y = -e_0 \cdot \left[(E_{yy0} + A_{ay} \cdot \Delta) \cdot \left(1 - \frac{(\Phi - \Phi_{Eyy})^2}{2} \right) \right] \\ +e_0 \cdot \left[(B_{yy0} + M_{yy} \cdot \Delta) \cdot \left(1 - \frac{(\Phi - \Phi_{Byy})^2}{2} \right) \right] v_x \end{aligned} \tag{21}$$

and plotting the angle calculated using the force in y-direction results in the curves displayed in figure 65.

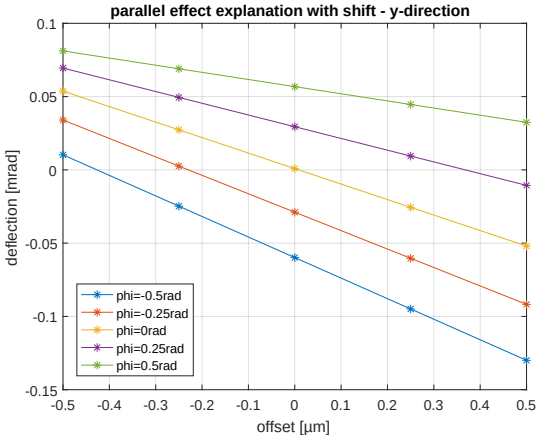

Figure 65: deflection with z-offset in y-direction with shift

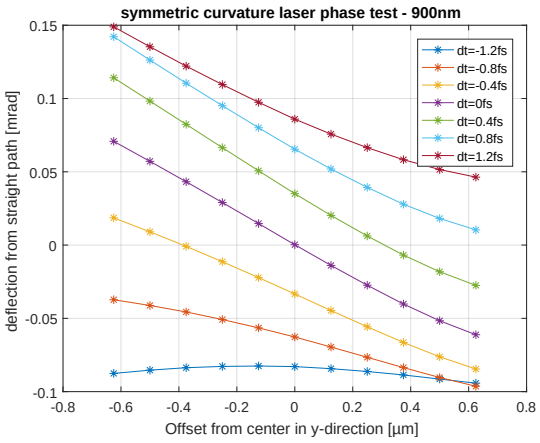

Figure 66: 2 μm symmetric curvature z-offset y-deflection laser phase test

For comparison the figure 66 shows the laser phase test in y-direction for a symmetric curvature dimension of 900 nm.

The most important insight of this curve is that the parallel effect is produced only by the difference of the shift in maxima of the electric and magnetic field. If the shifts are the same the parallel effect disappears. This is an interesting insight as first mathematical models did not account for the shift in amplitudes and therefore were not able to describe the desired effect. Overall the deflection results are similar and also the change in slope is described pretty well. Note that figure 66 plots a twice as high range in phase. The change in slope at higher offsets might be caused by the change in shift of maxima

at higher offsets, which was not accounted in the model. Further simulations will have to focus on finding a setup, where the shift in maxima is either the same or non existent.

11 Effect of the amount of pairs of pillars

All the previously presented tests were performed using 50 pairs of pillars. This is just an arbitrary amount since when doing experiments, the amount of pairs of pillars will be decided taking several factors into account like the typical offset of the particles, the focal length of the structure, the velocity and especially velocity gain, which leads to the dephasing length within the structure and also the fabrication possibilities. This section will focus on the deflection behaviour at different amounts of pairs of pillars and use the data for a wavelength of 2 μm and a 900 nm symmetric curvature as in section 8.3.

Typically one would expect the deflection to scale linearly with the amount of pairs of pillars. As displayed in figure 67 and 68 a pretty linear increase in deflection can be observed.

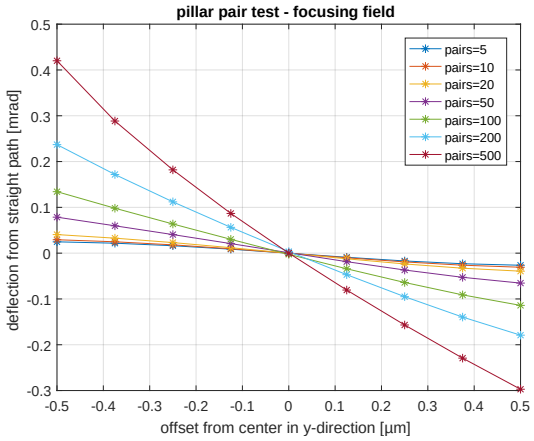

Figure 67: 2 μm pillar pair test y-direction

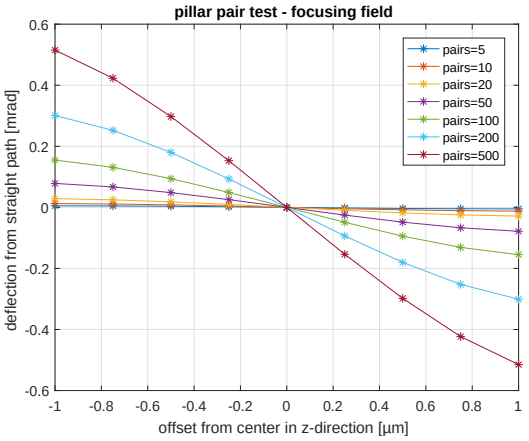

Figure 68: 2 μm pillar pair test z-direction

Though, the increase is not perfectly linear in both directions. While the deflection increases by about a factor 101 if increasing the amount of pairs from 5 to 500 in z-direction, in y-direction the deflection only increases by about a factor of 17. This could be explained by the change in position while propagating through the pillars. For example already after 50 pairs at a high offset the deflection angle is about 0.1 mrad. Even letting the particle propagate freely without the laser present would result in a change in position of

$$d = l \tan(\alpha) \tag{22}$$

where l is the free propagation length and α is the deflection angle. Assuming 500 pairs of pillars, the particle would propagate freely for 450 periods or 900 μm using a wavelength of 2 μm. Using the deflection angle of about 0.1 mrad after 450 pairs the particle would be about 90 nm closer to the centre and the closer the particle is to the centre the weaker the force gets. Integrating over the whole propagation distance the effect is actually worse than this simple calculation. Tests showed that after 500 pairs of pillars

with 1 μm offset in z-direction the particle is already 300 nm closer to the centre. On first sight, this might explain a decrease in linearity of the deflection.

The deflection in z-direction, instead, scales perfectly linearly. So, the change in position seems to be a minor effect. The main factor for the decrease in deflection in y-direction might be the effect of y-deflection at z-offsets as explained in section 10.1.2. This effect strongly increases as the amount of pairs of pillars increases. It is, as displayed in figure 63, negative for most offsets, but especially for zero offset and increases in magnitude as the the amount of pairs increases. To still hit zero deflection at zero offset, non perfect phase times of the laser, resulting in positive parallel effect, are needed to compensate the negative deflection. As non perfect laser phase times are used, the force is weaker.

Another reason for the worse scaling can be seen in the three sub-figures of figure 72. The deflection at different times from the perfect laser phase is displayed. One can easily see that for higher offsets a time difference of 0 fs does not hit the same points of the cosine like curve. While nearly the maximum is hit for 5 pairs of pillars, the deflection is close to the turning point for the 500 pair case. If always the maximum would be hit, the difference in deflection would be about a factor 35. So a combination of these two effects reduces the linearity.

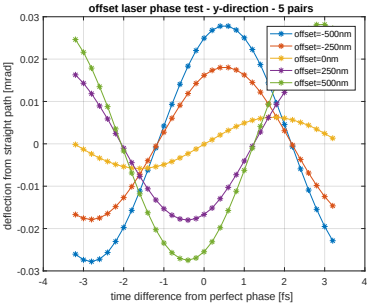

Figure 69: 5 pillar pairs

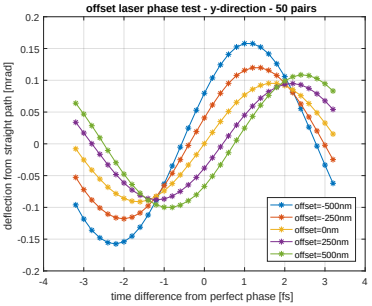

Figure 70: 50 pillar pairs

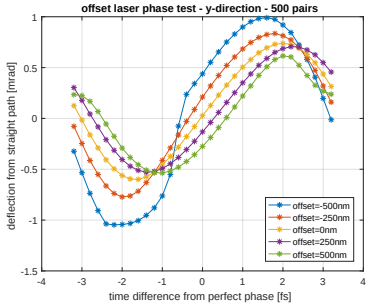

Figure 71: 500 pillar pairs

Figure 72: 2 μm pillar pair laser phase test y-direction

Apart from the general deflection strength as function of the amount of pairs of pillars, the arrival time effects can also be described by these curves. As displayed in figure 72 and 76 there is a strong difference between the pillar pair laser phase tests for the two directions. While in z-direction the curves for positive and negative offsets are mirrored, the curves at same phase in y-direction become more similar with higher amounts of pillars. Looking at these curves already shows, why the parallel effect only happens in y-direction. In z-direction, if the phase is changed, the curve of a positive offset decreases while the one with the negative offset increases or vice versa. Therefore only the slope changes. In y-direction especially for high amounts of pairs of pillars the curves for positive and negative offsets equally change. Therefore the difference between the

deflection for positive and negative offsets only slightly changes while the overall curve is shifted up and down at imperfect phase.

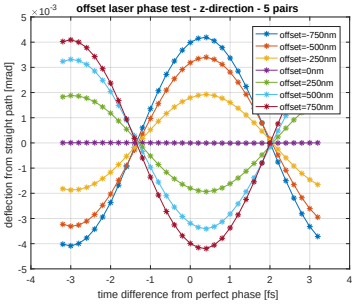

Figure 73: 5 pairs of pillars

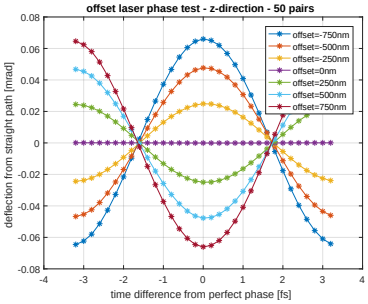

Figure 74: 50 pairs of pillars

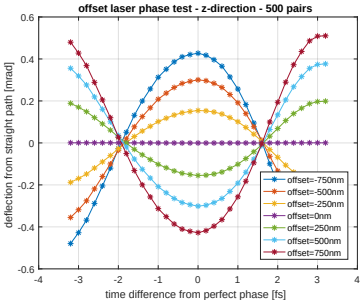

Figure 75: 500 pairs of pillars

Figure 76: 2 μm pillar pair laser phase test z-direction

Another observation for high amounts of pairs of pillars and high offsets in y-direction is that the curve is not as smooth. This is due to the fact that the particle's propagation is stopped when it exited the simulation volume in y-direction. So, using long particle bunches with high amount of pillars at high offsets could be a problem as already particles, which are half a femtosecond too early get deflected out of the propagation volume.

Therefore, it would be better to use a structure with a really strong deflection and only a few pillars than a weaker deflecting structure with a higher amount of pillars as the behaviour in z-direction does not change and the parallel effect in y-direction decreases.

12 deflection with offsets in both directions

So far only single directional offsets tests were conducted. Though, as for example section 10.1.2 showed, there are effects on the deflection behaviour of one direction, if the other is offset. To gain some insight on the effects two types of tests were conducted. The first test focused on the change in deflection for a z-direction offset if the particle has also an offset in the y-direction and vice versa. The second test focused on the deflection behaviour if a particle is offset diagonally from the centre. A diagonal offset means in both directions at the same time. As seen in figure 78, one offset step u means an offset of $0.25\,\mu$m in z-direction and $0.125\,\mu$m in y-direction. As always the biggest offsets were 5 or 6 steps depending on the wavelength in positive and negative direction. The first test focuses on exploring the coupling between the two directions, while the second focuses on a real life example, where particles will have offsets randomly distributed in y and z-direction. Both tests were conducted for both wavelength. For a wavelength of $2\,\mu$m a 900 nm symmetric curvature as in section 8.3 was used. As in section 7.2 the equivalent 1400 nm symmetric curvature setup was used for the $3.3\,\mu$m tests.

12.1 both directions offset test

The y-direction offset tests were conducted for offsets in z-direction ranging between $-1\,\mu$m and $1\,\mu$m and the ones in z-direction for y-offsets ranging between $-0.5\,\mu$m and $0.5\,\mu$m to cover the usual cases. The results for a wavelength of $2\,\mu$m are displayed in figure 77 and 78. The ones for a wavelength of $3.3\,\mu$m are displayed in figure 79 and 80. Comparing the two plots for y-direction offset tests it is pretty clear that positive and negative offsets in z-direction decrease the deflection in y-direction by about the same amount. For a wavelength of $2\,\mu$m the curves for negative z-offsets are completely hidden behind the positive ones. These effects are clearly linked to what has been described in section 10.1.2 as figure 63 displays perfect symmetric behaviour. The change in z-direction can not be described the same way as in y-direction as there is no deflection in z-direction if there is only an offset in y-direction. Though, the decrease might be explained by the fact that the field is non uniform in positive and negative y-offsets, especially very close to the pillars. As the effect is different for the two wavelengths, it is not fully clear what is the cause. There are not too many other options as tests have shown that only the electric and corresponding magnetic field in the Lorentz force are needed to justify the behaviour.

Overall there seems to be a strong difference in the deflection in y-direction especially with negative offsets. Future simulations could focus on a case where the deflection in y-direction hardly changes with z-offsets.

12.2 diagonal offset test

As in a real experiment, not only the general deflection is important, but also the behaviour of randomly positioned particles. The worst possible case for each unit area

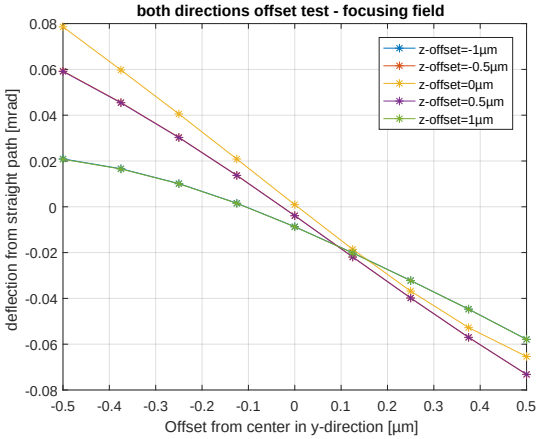

Figure 77: 2 μm both directions offset test y-direction

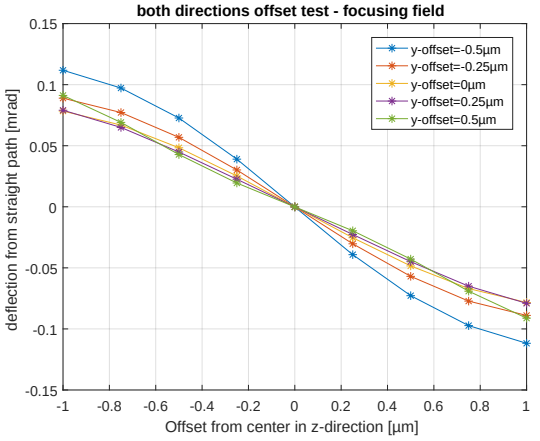

Figure 78: 2 μm both directions offset test z-direction

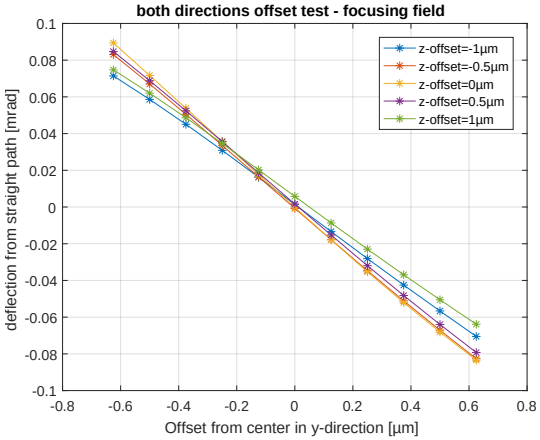

Figure 79: 3.3 μm both directions offset test y-direction

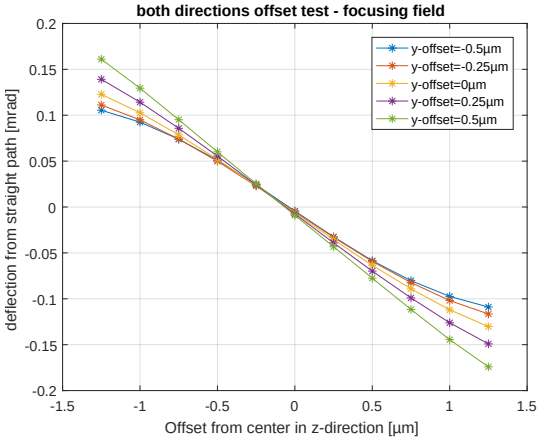

Figure 80: 3.3 μm both directions offset test z-direction

around the centre point is tested in the diagonal offset test. One unit of offset sets the particle 0.25 μm in z-direction and 0.125 μm in y-direction from the centre point. With this test it is crucial to look at deflections in both directions at the same time. In the focusing z cases the laser phase with the highest peak to peak deflection is chosen. Vice versa in the focusing y cases zero offset in y-direction is supposed to have zero deflection. Therefore, the corresponding laser phase is chosen. The results for a wavelength of 2 μm are displayed in figure 77 and 78. The ones for a wavelength of 3.3 μm are displayed in figure 79 and 80.
All figures show what is expected from a quadrupole like field. If there is focusing in z-directions there is defocusing in y-direction and vice versa. As the parallel effect is only present in y-direction and the appropriate laser phase is chosen, both the y-deflection and the z-deflection curve hit the centre point. In the z-deflection a strong difference in

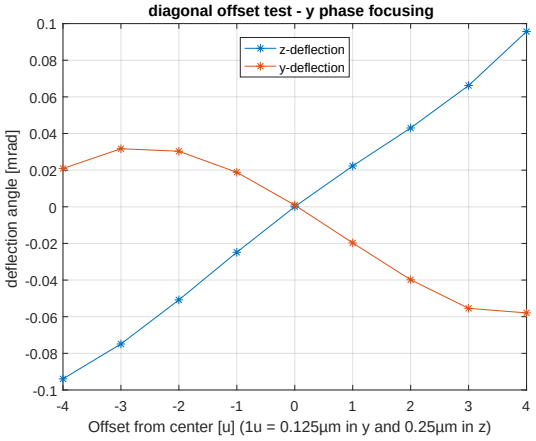

Figure 81: 2 μm diagonal offset test y-direction

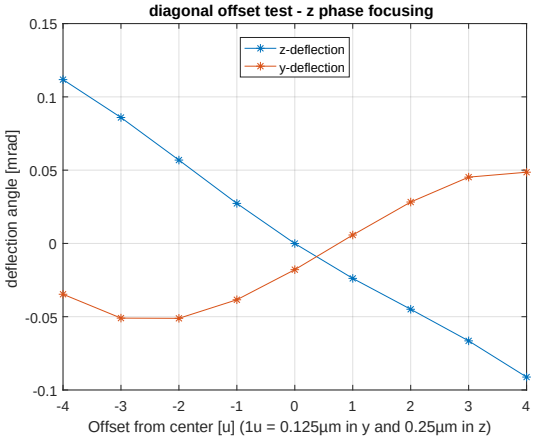

Figure 82: 2 μm both diagonal offset test z-direction

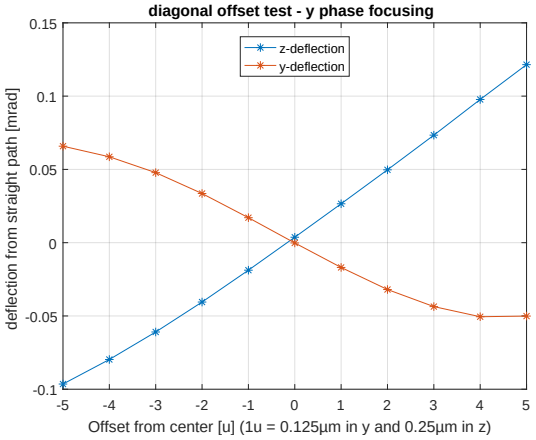

Figure 83: 3.3 μm diagonal offset test y-direction

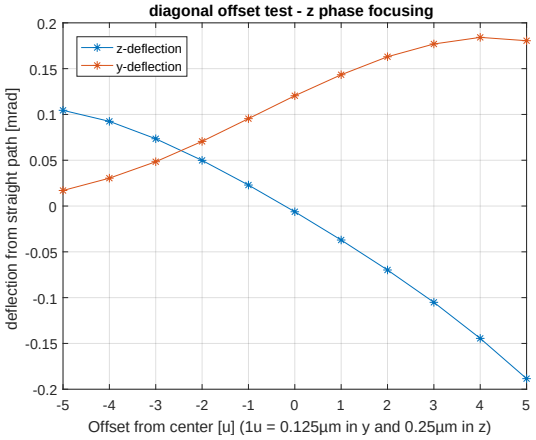

Figure 84: 3.3 μm diagonal offset test z-direction

parallel effect is visible. While the shift of the y-deflection curve is quite small in the 2 μm case, the shift is different in sign and really strong in the 3.3 μm case. This is another important effect observed during this thesis. The perfect laser phase for focusing z-direction and focusing y-direction are not always perfectly shifted by half a period. Usually only in a few setups the results look as good as in the 900 nm symmetric curvature case for a wavelength of 2 μm. A similar setup for a wavelength of 3.3 μm was the 1500 nm curvature b case.

Even after extensive research there is still no evidence that the shift between the perfect laser phase for y and z-direction can be determined without simulating, as this is mainly caused by the effect described in section 10.1.2. Though, as the two perfect laser phase times are shifted by half a period in the 900 nm symmetric curvature test, there are still

deflections visible. Even though no offset in y-direction, as seen in figure 63, it can not be assumed that without these effects, the shift between the two perfect laser phases would always be half periods. For real experiments, the structure will foremost have to focus on hitting a shift of half period otherwise particles will not behave as in a quadrupole. While focusing in z-direction will still be good, the behaviour in y-direction will depend strongly on the parallel effect shift. A tradeoff would be to only focus on the laser phase of the y-direction as the z behaviour would be the same just weaker.

13 Summary of the simulation results

As all aspects of the structure's deflection behaviour were tested, a summary of the findings follows. The key points are the optimisation process especially for highest deflection and best quadrupole like behaviour, the behaviour with different refractive indices and the description and cause of effects, which are not concluded by the optimisation process.

The results of the optimisation process clearly indicate that optimisation of the structure is highly desired as the difference in deflection between a randomly chosen setup and a highly optimal setup can easily be a factor 13 in z-direction and a factor 20 in y-direction for a wavelength of $2\,\mu$m. For a wavelength of $3.3\,\mu$m the increase in deflection in z-direction can be about a factor of 60, while it can be a factor of 26 in y-direction. This already proves that the optimisation increases the deflection significantly, but also shows that the possible increase is not uniform for different wavelengths and directions. The difference between the highest optimised deflection differed by a factor 2.4 in z-direction and a factor 1.6 in y-direction. So also the difference between the optimised deflections is not a factor 1.65 as expected from the increase in propagation length, but instead even better for the $3.3\,\mu$m case. As the refractive index is practically the same for both wavelengths there have to be some other reasons for this differences.

What was not presented in the optimisation sections, but was tested during this thesis was combining all the optimisation results. Most of the results were chosen for further tests anyway, but especially the height remained the same, even though slightly higher pillars showed stronger deflection. Exploring other cases with dimensions of the width $W = 600\,\text{nm}$, gap $G = 1.75\,\mu$m, height $H = 4.25\,\mu$m, symmetric curvature $C = 900\,\text{nm}$, shift $S = 700\,\text{nm}$ with the pillar head for a wavelength of $2\,\mu$m and dimensions of $W = 1100\,\text{nm}$, $G = 2.475\,\mu$m, $H = 7\,\mu$m, $C = 1400\,\text{nm}$, $S = 1500\,\text{nm}$ with the pillar head for a wavelength of $3.3\,\mu$m did not result in deflections higher than the presented cases. The deflections were higher than in all non shifted cases, but worse than the optimised shifted case. This leads to the conclusion that the parameters are very interlinked and a single parameter optimisation is only a first step towards the final structure. On one hand this is good, as this optimisation process probably lead to a local maximum of the deflection and there might be higher maxima of deflection out there. This might especially be true with curvature a and curvature b tests, as their are a lot of combinations untested. On the other hand this also leads to the conclusion that the current highest deflection case has to be thoroughly tested for changes in dimensions, which will definitely occur during fabrication as already a small change in height had drastic effects on the results.

Apart from all the tests conducted during this thesis, there are still a lot more possible tests that could be studied to get a final understanding of the structure's behaviour. One type of tests would be to combine two parameter dimensions to an interlinked one. Starting with parameters which stretch in the same direction, is definitely advisable. More refined optimisations could also be foreseen. Examples are the width and the gap

between the pillars or the combination of curvature a and the height. These tests might bring an understanding into the question, why a pillar, which is slightly higher than two times the wavelength results in drastically higher deflections or why the best pillar gap case for the two tested wavelengths is different. Also, it is not clear why height and gap behave differently in the structure. One could assume that their behaviour should be the same. Some tests should be conducted testing even higher pillars gaps in the range of two times the wavelength as there is an indication of slightly higher than one wavelength for the height too. Also four times the wavelength could be tested for the height. Another interlink could be curvature b and the shift as they both stretch in x-direction. Other types of new tests would include comparisons if a different amount of pairs of pillars influences the optimisation process. Generally this is not expected, but as displayed in figure 72 for the pillar pair tests, the deflection changes a lot with the amount of pairs of pillars and does not scale linearly in y-direction. There might be different optimisation cases for different amounts of pairs of pillars to make the y-deflection scale better. This is especially important, if a higher amount of pairs of pillars is used in experiments as a small change in optimisation per period increases the overall deflection and an increase in linearity would even more drastically increase the deflection.

As a high deflection alone does not lead to great focusing results, the behaviour of the the deflection at imperfect laser phase became a great tool. The laser phase tests, even though not presented for each case, sometimes show more drastic changes in the deflection behaviour than the deflection plots reveal. Especially in the shifted pillar setups the parallel effect could be decreased a lot while at the same time increasing the overall deflection. Decreasing the parallel effect is especially important as the stronger the parallel effect is compared to the maximum deflection, the more accurate the perfect laser phase will have to be hit in future experiments to assure the desired focusing effects. Though, not only the strength of the parallel effect is important, but also the shift between the perfect laser phase for the two directions is important. Tests have shown that several optimisation setups show different shifts. It would be desirable to have no shift at all between the perfect laser phase for focusing in one direction and defocusing in the other direction. This also shows that shifts between the perfect laser phase do not especially occur neither for high deflection setups nor for low deflection setups.

It was also shown that the two directional offset tests influence each other. The coupling increases as the number of pillar pairs increased. Decreasing this effect is important as it directly decreases the deflection in y-direction and at the same time, shifts the parallel effect which has to be compensated with different laser phase, inherently resulting in an even further decrease in deflection.

The few tests conducted with different refractive indices show no promising results. This will make the whole process more complicated as for each new material with a different refractive index the optimisation will have to be redone. More thorough tests with the refractive index are advised. It would be interesting to fully optimise the structure for at least another different refractive index to see how different the optimal structure

is from the current results. This way it would be possible to draw parallels between the two refractive indices and possibly find solutions to other unsolved questions about why the structure behaves the way it does.

14 Fabrication results

Optimisation and simulation of the structure is only one step towards a full experiment. As PSI had worked on similar structures with straight pillars before and have them produce by FEMTOprint, the idea was to produce the curved pillar structure in a similar way. They describe their technology [28] as:

> FEMTOPRINT® technology uses a femtosecond laser that changes the properties of glass in the focal point with a sub-micron resolution. With the modified refractive index, optical paths can be written in the glass. Wet etching removes the written part forming complex 3D structures with high aspect ratio and high precision.

The material of the fabricated structure would therefore be glass or fused silica, hence the choice of material in the simulations [22]. Quite early in the optimisation process FEMTOprint was contacted and a first design proposal was sent to them. Though, it was clear quite soon that FEMTOprint would not be able to produce the curved pillars for the nominal 2 μm ACHIP wavelength. Since laser acceleration with a wavelength of 150 μm is also conducted at PSI some samples for this wavelength were ordered. The results are displayed in figure 85. The results look really promising and statistics on the different parameter dimensions also promises good fabrication accuracy. If this fabrication process can be optimised in the coming years to fabricate smaller structures, as this setup is currently about 45 times bigger than what would be needed for the 3.3 μmu structures and 75 times bigger than what would be needed for the 2 μm structures, this could become a really cost efficient way to mass produce acceleration and focusing structures.

As fabrication with FEMTOprint was not possible for shorter wavelengths a different fabrication method had to be found. A high precision 3D printer from Nanoscribe [29] is available at PSI and therefore tests with this device have been conducted. The results are displayed in figure 86 for a wavelength of 3.3 μm. This is far from perfect but as this was just one test, fabrication optimisation could result in usable pillars. One problem still would be to determine the optical properties of the IP-dip [30] polymer used in the fabrication.

Although the first samples are far from perfect and still a lot of time will have to be invested in mass fabrication, these first fabrication tests still showed that current fabrication techniques are close to producing the needed structure dimensions and could become available in the near future. Once the issues while fabrication are known, simulation can focus on the most crucial parameters.

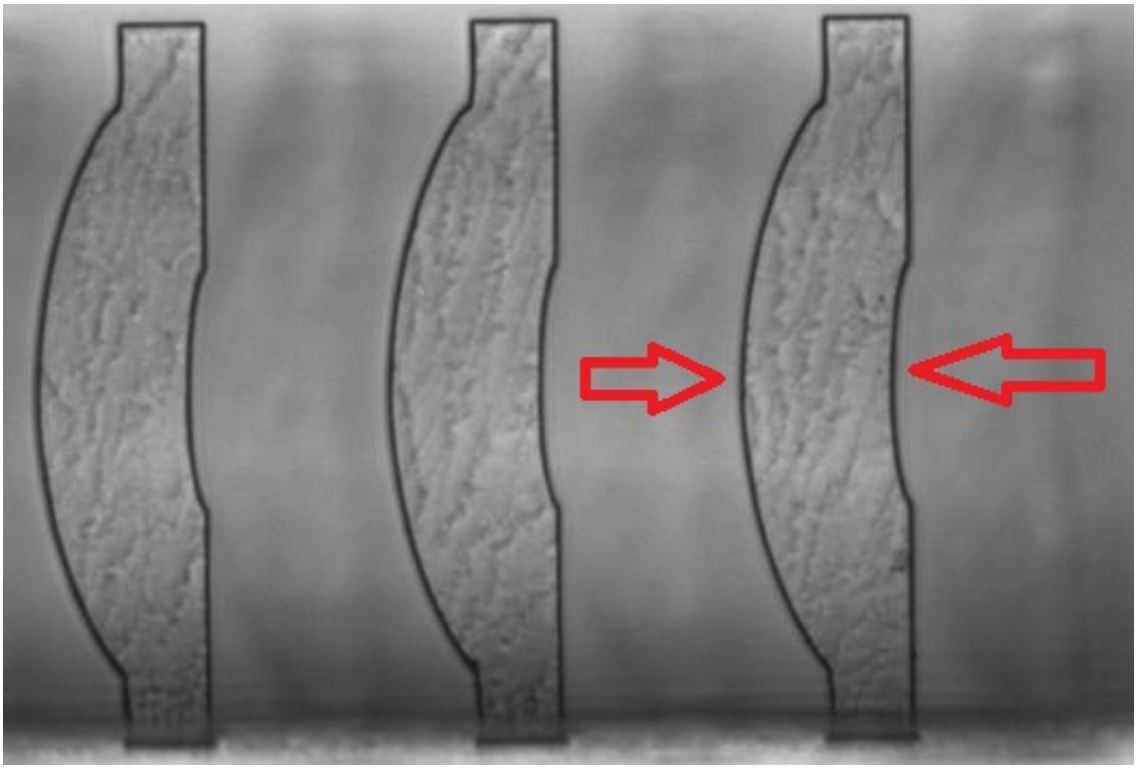

Figure 85: sample structure fabricated by FEMTOprint

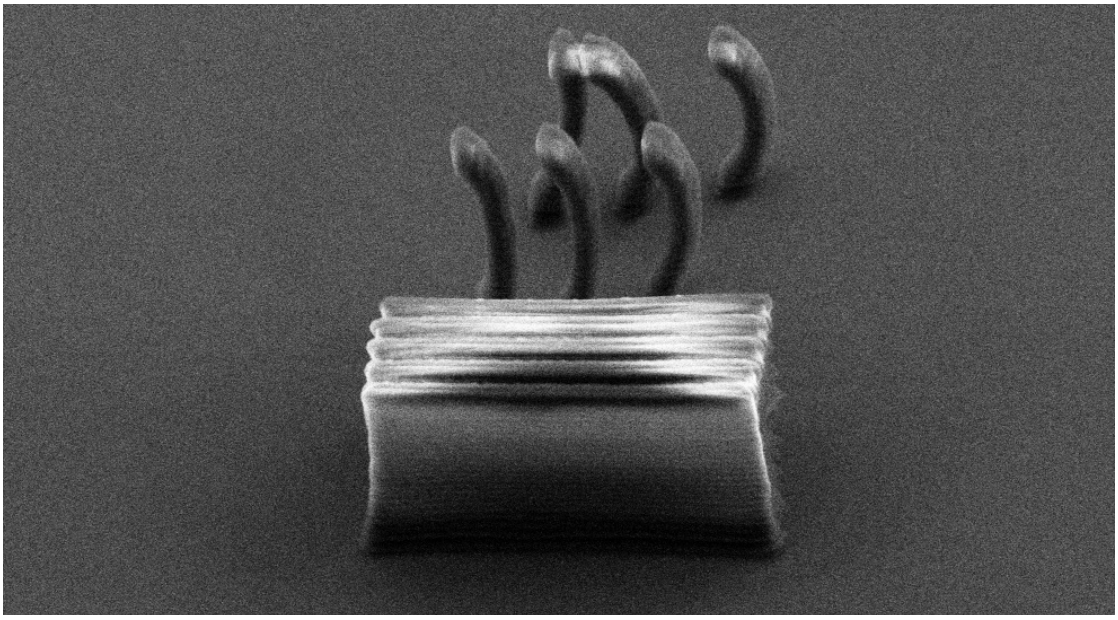

Figure 86: first fabricated pillars from the Nanoscribe device

15 Experiment setup

Once the simulations are complete and the fabrication of the structure works as planned, it would be necessary to verify if the simulations reproduce the results from the experiment. This section will focus on what a simple experiment could look like. As the two directions behave differently two possible experimental setup ideas have been developed. The setup consists of an appropriate amount of pairs of pillars, some free space to propagate, a wall with 5 holes and detectors behind the 5 holes. A sample design was constructed in Autodesk Inventor and is displayed in figure 87 and 88. The experiment was designed to be conducted at Friedrich Alexander University Erlangen at the Chair of Laser physics [17] in the ACHIP group [18] with Joshua McNeur.

The particle will propagate through the pillars, keep their angle and speed while propagating through vacuum and hit the wall with the holes. If the laser is switched off, the particles will keep their initial angle. Therefore the particle bunch will spread. If the spread is taken into account and the diameter of the apertures is chosen according to the spread, all particles will be detected by the centre detector regardless if the particles were offset from the centre or not. If the laser is switched on there are two possibilities. Either it is run in focusing phase or in defocusing phase. This experiment is created for defocusing phases. As the particle bunch width at about 50 nm is really small compared to the offset, the deflection angle at the end of the pillars will mainly depend on the initial offset. The outer holes' distances from the centre are determined by the deflection angle at highest offsets according to

$$\begin{aligned} d_h &= l \cdot \tan \Phi_h \\ d_v &= l \cdot \tan \Phi_v \end{aligned} \tag{23}$$

where l is the distance of free propagation between the last pillar and the wall, d_h is the horizontal distance from the centre of the centre aperture to the centre of the horizontal outer apertures, d_v is the vertical distance to the vertical outer apertures, Φ_h is the angle in y-direction and Φ_v is the angle in z-direction.

The experiment will start with particles without any offset from the centre. In this case there should hardly be any particles in the outer apertures and the highest detection in the centre aperture. The more the particles are offset from the centre the higher the amount of particles in the respective outer aperture will be and the lower the detection at the centre aperture will be. If the simulated maximum deflection angles are correct also in the experiment, then at maximum offset the whole particle bunch should be detected at the respective outer aperture. These offsets test will be conducted in both directions each for positive and negative offsets. Using the amount of recorded particles in the apertures the mean distance of the particles from the centre aperture for each offset can be calculated. Using equation 23 the mean distance from the centre can be used to calculate the mean angle of the particles at the exit of the structure. These angles can be plotted like the deflection plots from the simulations and should give similar results.

The advantage of the proposed setup is that offsets in both directions can be tested. In this case one direction would defocus and the other focus. If there is enough propagation space the particle's position in focusing direction will cross the centre point and be deflected outwards too. If the initial offset together with the amount of detected particles in the centre aperture and two outer apertures is taken into account, even the results from the bidirectional offset tests or diagonal offset tests could be verified.

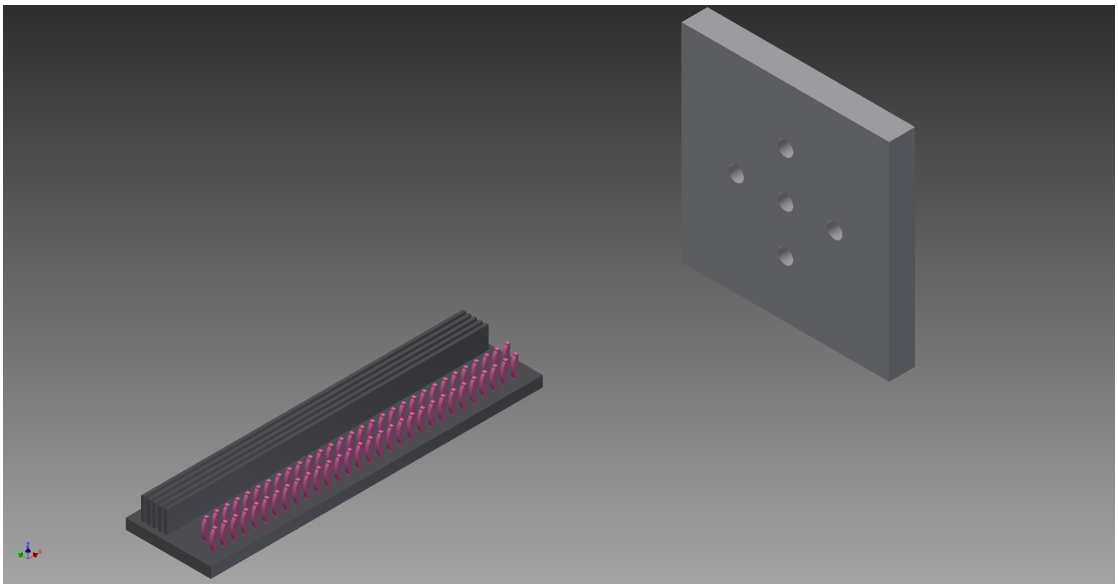

Figure 87: design of the experiment setup in Inventor

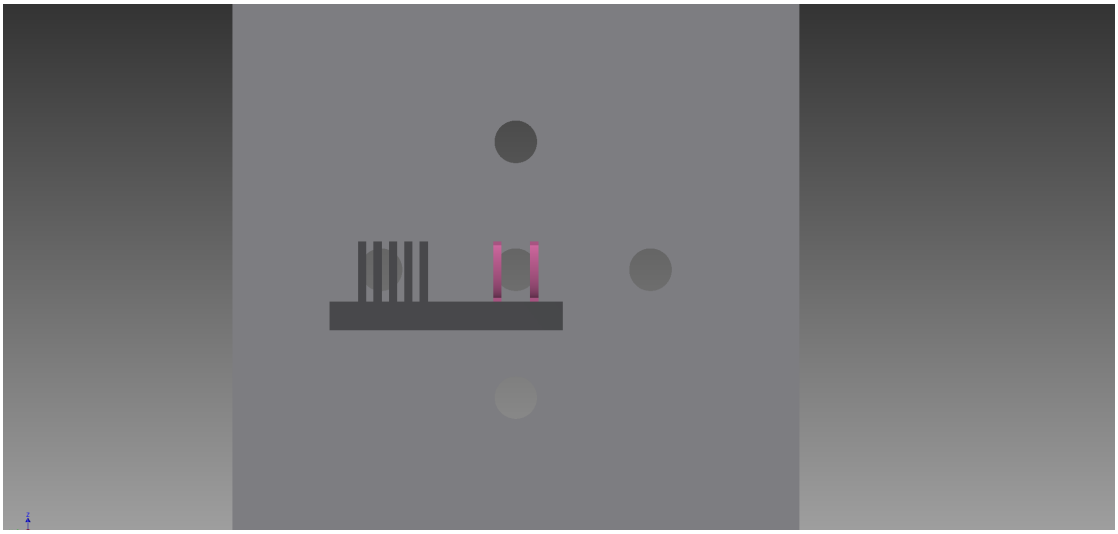

Figure 88: front view of the experiment to see the symmetric arrangement

16 Perspective

With the great results that were achieved during this thesis it is important to summarise all the crucial points and give a quick outlook on what future research will have to focus on.

The curved pillars are a great model to continue the concept of the straight pillars used for acceleration of particles. They combine relatively low focal length with great scalability through the laser's power output and a relatively easy optimisation process. The biggest issue of the curved pillars is still the overhang of the curvature. While straight pillars can easily be produced using for example photolithography [3] as their cross section does not change, with changing cross sections standard photolitography or 3D printing techniques have major problems fabricating the structure while satisfying the desired accuracies. So far fabrication at these small wavelengths is not feasible for most fabrication techniques. So, while fabrication techniques improve it might be interesting to look into more regular structures like the checkerboard structure proposed by Kent Wootton [2] for its less fragile setup.

Fabrication in general is an even bigger issue than it might seem in this thesis as all simulations were conducted for ultra-relativistic electrons at 0.9999 times the speed of light. A start to end concept [3] will require focusing structures at lower velocities. Using the current design of the focusing structure, the pillars would have to move closer together depending on the velocity to avoid dephasing problems. At for example half the speed of light, the distance between two pairs of pillars would only be half the wavelength compared to one wavelength as in the current simulations. This puts even more pressure on fabrications as at least the distance between two pillars will have to be decreased. Though, there is also the possibility that dimensions of other parameters will have to be changed too. What also should not be forgotten is that at lower velocities the gain in velocity in the particles propagation direction will be far bigger than at ultra-relativistic velocities leading to possible shortening of distances between pillars as the particle energy increases. Fabrication will have to be extremely accurate to include these changes in distance with high enough accuracy to avoid dephasing. One solution can be the use of higher harmonics of the structure itself. For the possible experiments that would have been conducted, if fabrication would work out, Joshua McNeur suggested to use up to the fourth harmonics of the structure. This thesis put some time looking into harmonics focusing, but the idea was put on hold as it turned out that fabrication is a limitation.

The combination of Autodesk Inventor for design, Lumerical for electromagnetic simulations and the particle tracking code in Matlab worked really well during this thesis, but it definitely has its limitations. One of the limitations in the current setup is that all the simulations were done using one unit cell consisting of two pillars and the Bragg reflector. More accurate simulations will also have to take into account the effects of the first and the last pillar pair, as using periodic boundary conditions is just an approximation. Another big limitations is that particle tracking was performed only with one particle at

a time. This neglects the contribution of space charge which is critical for high current beams. While future research might still use Inventor to design the structure, the electromagnetic simulations in Lumerical will become more complex. Current simulations for one unit cell took about 15 minutes per simulation. Doing electromagnetic simulations of a whole 50 pillar setup will therefore at least take 750 minutes and will not fit into RAM. Therefore, the electromagnetic simulations will have to be ported to a Cluster. Also the particle tracking code in Matlab will have to be modified. While in one way it would get less complex as repeatedly using the same dataset would vanish, the overall data sizes would increase drastically. This could lead to the need of partially loading the data into RAM. Apart from technical uncertainties, it will also be interesting to expand the code to send whole particle bunches with up to several hundred particles at different starting velocities, angles and phases described by different types of distributions through the focusing structure to see a statistical behaviour of the particle's propagation in situation closer to reality. Performing the proposed experiment in section 15 will be crucial to get a better understanding of what to expect and to cross check the simulations.

Optimisation of two different wavelengths has been conducted exhaustively. Apart from some further thorough tests that might or might not lead to stronger overall deflection as described in section 13, coupling of optimisation parameters is the only big issue. What is more important is the behaviour of different refractive indices as this did not scale in the conducted tests. Future simulations will have to focus on a material with a different refractive index to be able to draw conclusions on what causes the best deflection results.

The mathematical model was able to describe the general behaviour of the deflection curves really well. Future work should focus on two parts of the model. First is to resimulate the required electric and magnetic field amplitudes for different dimensions of the parameter to get a better understanding about which parts of the mean electric and magnetic field curves have the larger impact for the change in slope and parallel effect. Second, it would be interesting to link a change in dimension of one of the parameters to changes in the mean electric and magnetic field curves.

If several of the other questions are answered, it would be important to assess the possibilities of such focusing structures in a start to end setup of a compact table top accelerator. Most important would be to be able to create, similar to conventional accelerators, FODO like structures even though this seems to be more complicated than in the conventional design [31]. A full simulation of a FODO like structure would even help to improve the theoretical model of transfer matrices in dielectric focusing structures.

References

[1] ACHIP, "Research highlights." https://achip.stanford.edu/research-highlights. [accessed 2017-11-24].

[2] W. et al., "Dielectric laser acceleration and focusing using short-pulse lasers with an arbitrary laser phase distribution." http://aip.scitation.org/doi/abs/10.1063/1.4975868, March 2017.

[3] K. Wootton *et al.*, "Towards a Fully Integrated Accelerator on a Chip: Dielectric Laser Acceleration (DLA) From the Source to Relativistic Electrons," in *Proc. of International Particle Accelerator Conference (IPAC'17), Copenhagen, Denmark, 14th May, 2017*, no. 8 in International Particle Accelerator Conference, (Geneva, Switzerland), pp. 2520–2525, JACoW, May 2017. https://doi.org/10.18429/JACoW-IPAC2017-WEYB1.

[4] S. N. A. Laboratory, "Dielectric laser acceleration group." https://portal.slac.stanford.edu/sites/ard_public/aard/dla/Pages/Default.aspx. [accessed 2017-11-08].

[5] A. Stanford, "Accelerator on a chip international program." https://achip.stanford.edu/. [accessed 2017-11-08].

[6] A. Switzerland, "Laser acceleration on a chip." www.achip.ch. [accessed 2017-11-08].

[7] C. K. Birdsall and A. B. Langdon, *Plasma physics via computer simulation*, ch. 4 and 15, pp. 58–63 and 356–357. Adam Hilger, 2nd ed., 1991.

[8] J. M. et al., "Elements of a dielectric laser accelerator." https://arxiv.org/abs/1604.07684, April 2016.

[9] A. Inc, "Inventor." https://www.autodesk.com/products/inventor/overview. [accessed 2017-11-12].

[10] L. Inc, "Fdtd solutions." https://www.lumerical.com/tcad-products/fdtd/. [accessed 2017-11-07].

[11] T. M. Inc, "Matlab." https://uk.mathworks.com/products/matlab.html. [accessed 2017-11-08].

[12] K. Shimoda, "Proposal for an electron accelerator using an optical maser," *Appl. Opt.*, vol. 1, pp. 33–35, Jan 1962.

[13] P. Soong et al., "Demonstration of electron acceleration in a laser-driven dielectric microstructure," *nature*, vol. 503, pp. 91–94, 2013.

[14] J. Breuer and P. Hommelhoff, "Laser-based acceleration of nonrelativistic electrons at a dielectric structure," *Phys. Rev. Lett.*, vol. 111, p. 134803, Sep 2013.

[15] J. Harrison, Y. Hwang, O. Paydar, J. Wu, E. Threlkeld, J. Rosenzweig, P. Musumeci, and R. Candler, "High-gradient microelectromechanical system quadrupole electromagnets for particle beam focusing and steering," *Phys. Rev. ST Accel. Beams*, vol. 18, p. 023501, Feb 2015.

[16] E. Prat, S. Bettoni, M. Calvi, M. Dehler, F. Frei, P. Hommelhoff, M. Kozak, J. McNeur, C. O. Loch, S. Reiche, A. Romann, and R. Ischebeck, "Outline of a dielectric laser acceleration experiment at swissfel," *Nuclear Instruments and Methods in Physics Research Section A: Accelerators, Spectrometers, Detectors and Associated Equipment*, vol. 865, no. Supplement C, pp. 87 – 90, 2017. Physics and Applications of High Brightness Beams 2016.

[17] F. Erlangen, "Chair for laserphysics." `https://www.laserphysics.nat.fau.eu/`. [accessed 2017-11-24].

[18] F. Erlangen, "Achip: Electron acceleration with laser light." `https://www.laserphysics.nat.fau.eu/research/achip/`. [accessed 2017-11-24].

[19] W. Demtröder, *Experimentalphysik 2*, ch. 10, pp. 311–312. Springer, 2nd ed., 2002.

[20] D. Chakravorty, "Stl file format for 3d printing." `https://all3dp.com/what-is-stl-file-format-extension-3d-printing/`. [accessed 2017-11-12].

[21] D. Cruz-Uribe and C. Neugebauer, "Sharp error bounds for the trapezoidal rule and simpson's rule." `http://www.emis.de/journals/JIPAM/images/031_02_JIPAM/031_02.pdf`. [accessed 2017-11-13].

[22] E. D. Palik, *Handbook of Optical Constants of Solids*, vol. 1, pp. 719–747. 1997.

[23] S. G. Johnson, "Notes on perfectly matched layers (pmls)." `http://math.mit.edu/~stevenj/18.369/pml.pdf`. [accessed 2017-11-07].

[24] NIST, "International system of units (si)." `https://physics.nist.gov/cuu/Units/`. [accessed 2017-11-15].

[25] J. P. Boris, "Relativistic plasma simulation-optimization of a hybrid code," *Proceeding of Fourth Conference on Numerical Simulations of Plasmas*, November 1970.

[26] W. Demtröder, *Experimentalphysik 2*, ch. 7, pp. 191–192. Springer, 2nd ed., 2002.

[27] J. Hasenbichler, "Shared plots." `https://drive.switch.ch/index.php/s/MuuQ8Zcf525aM6o`. [accessed 2018-01-07].

[28] FEMTOprintSA, "Femtoprint." `https://www.femtoprint.ch/`. [accessed 2017-11-23].

[29] N. GmbH, "Nanoscribe." `https://www.nanoscribe.de/en/`. [accessed 2017-11-23].

[30] N. GmbH, "Ip photoresists." `https://www.nanoscribe.de/en/products/ip-photoresists/`. [accessed 2017-11-23].

[31] A. Szczepkowicz, "Application of transfer matrix and transfer function analysis to grating-type dielectric laser accelerators: Ponderomotive focusing of electrons," *Phys. Rev. Accel. Beams*, vol. 20, p. 081302, Aug 2017.